

Tutorial on narrow linewidth tunable semiconductor lasers using Si/III-V heterogeneous integration ^F

Cite as: APL Photonics 4, 111101 (2019); <https://doi.org/10.1063/1.5124254>

Submitted: 13 August 2019 • Accepted: 11 October 2019 • Published Online: 05 November 2019

 Minh A. Tran, Duanni Huang and John E. Bowers

COLLECTIONS

Paper published as part of the special topic on [Hybrid Integration beyond Silicon Photonics](#)

 This paper was selected as Featured



View Online



Export Citation



CrossMark

ARTICLES YOU MAY BE INTERESTED IN

[Perspective: The future of quantum dot photonic integrated circuits](#)

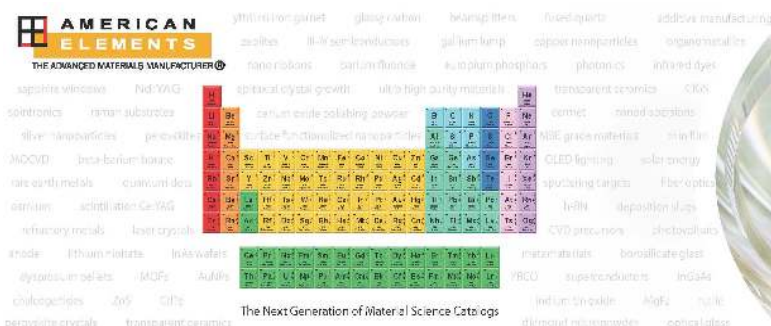
APL Photonics 3, 030901 (2018); <https://doi.org/10.1063/1.5021345>

[Hybrid and heterogeneous photonic integration](#)

APL Photonics 6, 061102 (2021); <https://doi.org/10.1063/5.0052700>

[Low noise, tunable silicon photonic lasers](#)

Applied Physics Reviews 8, 031306 (2021); <https://doi.org/10.1063/5.0046183>



Tutorial on narrow linewidth tunable semiconductor lasers using Si/III-V heterogeneous integration

Cite as: APL Photon. 4, 111101 (2019); doi: 10.1063/1.5124254

Submitted: 13 August 2019 • Accepted: 11 October 2019 •

Published Online: 5 November 2019



Minh A. Tran,^{1,2,a)}  Duanni Huang,^{1,3,a)} and John E. Bowers^{1,b)}

AFFILIATIONS

¹Electrical and Computer Engineering Department, University of California, Santa Barbara, Santa Barbara, California 93106, USA

²Nexus Photonics, LLC, Santa Barbara, California 93106, USA

³Intel Labs, Santa Clara, California 95054, USA

Note: This article is part of the Special Topic on Hybrid Integration beyond Silicon Photonics.

a) Contributions: M. A. Tran and D. Huang contributed equally to this work.

b) bowers@ece.ucsb.edu

ABSTRACT

Narrow linewidth lasers have many applications, such as higher order coherent communications, optical sensing, and metrology. While semiconductor lasers are typically unsuitable for such applications due to relatively low coherence, recent advances in heterogeneous integration of III-V with silicon have shown that this is no longer true. In this tutorial, we discuss in-depth techniques that are used to drastically reduce the linewidth of a laser. The heterogeneous silicon-III/V platform can fully utilize these techniques, and fully integrated lasers with Lorentzian linewidth on the order of 100 Hz and tuning range of 120 nm are shown.

© 2019 Author(s). All article content, except where otherwise noted, is licensed under a Creative Commons Attribution (CC BY) license (<http://creativecommons.org/licenses/by/4.0/>). <https://doi.org/10.1063/1.5124254>

I. INTRODUCTION

The primary advantage of silicon photonics is the extremely mature silicon manufacturing ecosystem that is a result of decades of CMOS development.¹ By leveraging this, silicon photonics has developed at a rapid rate, as much of the infrastructure was already present in terms of wafer availability, process technology, and equipment. While photonics cannot follow the exact same path as electronics since optical elements cannot be scaled the same way the transistor has been miniaturized, it has found other ways to scale. For example, the development of ring resonators has led to the miniaturization of certain components such as modulators, lasers, and filters.^{2–4} High fabrication yield and novel device designs have also led to a scaling in complexity and functionality. Over the past few decades, silicon photonics has matured from early concepts^{5,6} to single device level demonstrations to large scale photonic integrated circuits (PICs) containing thousands of photonic elements. In addition, cheaper material costs and larger wafer sizes have propelled silicon photonics to be the leading candidate for large volume

production. A typical silicon wafer is 300 mm in diameter, while the largest III-V wafers tend to be 100 or 150 mm in diameter. Thus, over the past decade, silicon photonics has established a firm foothold in the data center market^{7–9} and is also an active competitor in emerging applications such as spectroscopy, LiDAR, deep learning, and quantum applications.^{10–17}

In addition to economic benefits, there are a number of performance benefits when considering silicon photonics. One benefit is from the silicon waveguide itself. The silicon on insulator (SOI) platform is a high index contrast platform, with the refractive index difference between the core silicon waveguide and surrounding oxide cladding approximately equal to 2. This high index contrast enables low-loss bends in the waveguide on the order of several micrometers as well as extremely compact power splitters, multiplexers and demultiplexers, grating couplers, and polarization diversity components.^{18–20} At the same time, high index contrast waveguides require precise fabrication, as the waveguides become very sensitive to variation. For SOI wafers, the top device layer thickness is a crucial parameter, and its uniformity has improved with larger wafer size.

Photolithography for 300 mm wafers is also state of the art, which directly has implications in terms of waveguide loss and uniformity.^{21–23} Global Foundries have reported waveguides in a 300 mm platform to have half the variation in loss compared with 200 mm wafers,²⁴ while IMEC has seen similar improvements in waveguide width and height variation by moving to 300 mm.²⁵ Meanwhile, Intel has shown that tight process control in its 300 mm silicon fab can accurately target the lasing wavelength across an entire wafer to be on the order of 0.3 nm.²⁶ Finally, SOI wafers have very few defects, which is also an advantage when considering waveguide performance and yield.

Despite these advantages in passive photonic elements, silicon faces some challenges when considering active photonic elements such as lasers, modulators, and photodetectors. A purely silicon platform has limited functionality and may not meet the demands of multifunctional PICs. Silicon modulators operating based on carrier depletion are commonly used today^{27,28} but do not have the best performance in terms of modulation bandwidth, phase efficiency, or loss. Silicon can also be used as a photodetector at the commonly used telecom wavelengths (1310 nm and 1550 nm), using a combination of two photon absorption, defect absorption, and other effects.^{29–32} However, the material is still sub-bandgap at these wavelengths, meaning that they do not absorb as efficiently as III-V or germanium detectors. While silicon-based detectors and modulators are not optimal in terms of performance, they are still used due to the high level of integration with the rest of the silicon photonic platform. In other words, the manufacturing advantages of silicon photonics outweigh the performance penalty for many applications.

However, there is no trade-off to be made when it comes to lasers. Silicon is an indirect bandgap material and therefore completely unsuitable as an efficient gain medium for lasers. While germanium lasers on silicon have been demonstrated, their efficiency is not sufficient for most practical applications.^{33,34} Thus, III-V materials (InP, GaAs, etc.) with a direct bandgap provide the only realistic solution for the laser, but their integration on silicon is not straightforward. Monolithic approaches are desired, and tremendous progress has been made using quantum dots as gain materials, but certain challenges still exist, such as the coupling of the light from the quantum dot layer into the silicon waveguide layer.^{35–40} The more commonly used approaches as of today are hybrid integration of silicon and III-V, where the III-V laser is flip-chip bonded or otherwise assembled along with the silicon PIC, or heterogeneous

integration, in which an unprocessed III-V die is directly bonded on top of the silicon waveguides.⁴¹ Both approaches gain the flexibility of using the optimized III-V material for gain and active components, and silicon waveguides for passives. The primary differentiator between the two approaches is the potential for scalability. Heterogeneous integration is compatible with 300 mm wafer-level processing, as evidenced by Intel's heterogeneous silicon photonic process.²⁶ On the other hand, each chip in hybrid integration must be individually assembled, often with stringent alignment tolerance. Thus, heterogeneous integration of III-V on silicon is more suitable for mid to large volume applications. Another key distinction between the two is the increased susceptibility to shock and vibration for hybrid devices. This is particularly important in the area of optical sensors, for which a heterogeneous approach would be preferred.

From a performance standpoint, both hybrid and heterogeneous silicon/III-V lasers have several advantages compared with monolithic III-V only platforms. For example, multiple die bonding offers the ability to incorporate different gain materials or optimized gain, modulator, and photodetector materials onto the same silicon photonic PIC without significantly increased fabrication complexity.^{42–44} Similarly, hybrid lasers with multiple gain chips coupled to a single silicon PIC have been demonstrated.⁴⁵ In monolithic III-V platforms, multiple regrowth steps are needed, which is costly and decreases the yield. Heterogeneous integration captures the best out of both worlds, as it provides significantly more flexibility compared with a monolithic III-V approach, while retaining the scalability that silicon photonics provides.

While multiple papers have been published on the heterogeneous silicon platform, the variety of materials that can be integrated on it (Fig. 1), and the advantages it holds,^{46–50} this tutorial will be focused on one application, which is the low-noise, narrow linewidth semiconductor laser. Traditionally, monolithic III-V semiconductor lasers have not demonstrated the narrow linewidth, with the best lasers in the tens of kilohertz, and most lasers in the megahertz range. Low noise semiconductor lasers are useful in many areas such as coherent communications, RF photonics, and coherent sensing. The common requirements for the laser in these fields are low relative intensity noise (RIN) and low frequency noise (linewidth).

To get into the single kilohertz range and below, fiber and solid-state lasers are used.^{51–54} Such lasers are bulky and very expensive compared with semiconductor lasers. To bridge the gap,

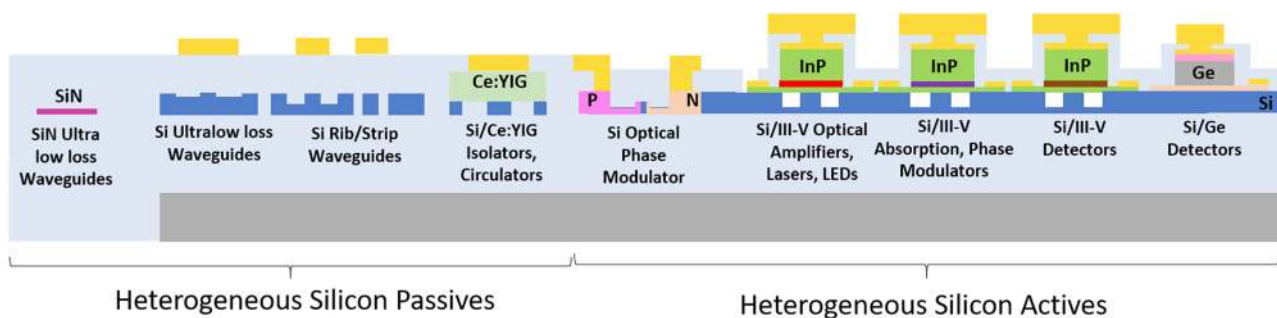


FIG. 1. The heterogeneous silicon platform has flexibility to incorporate III-V and otherwise incompatible materials onto 300 mm silicon wafers. Device performance can be optimized without sacrificing the potential for scalability.

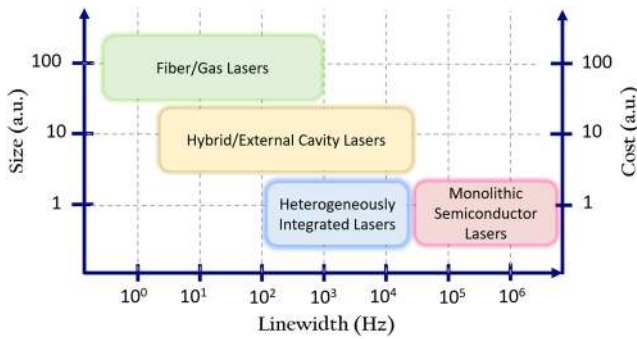


FIG. 2. Summary of the general metrics for narrow linewidth lasers. Heterogeneously integrated lasers have the potential to match hybrid and external cavity lasers in performance without an increase in size and cost.

external cavity lasers using semiconductor gain chips with long, low-loss optical delays are used. These external cavities are comprised of fibers or external crystalline whispering gallery resonators and Fabry-Perot etalons.^{55–57} More recently, integrated external cavities using the aforementioned hybrid integration to assemble multiple semiconductor chips have been used to further reduce the cost and size of such lasers.^{58–62} Here, the superior passive performance of silicon or silicon nitride waveguides has a direct benefit in reducing the noise of the laser. In this work, heterogeneously integrated lasers are shown to provide much of the same benefits in terms of linewidth reduction, while maintaining cost and footprint similar to monolithic III-V semiconductor lasers. These relevant metrics are given in Fig. 2, and a number of results are highlighted in Fig. 3. State of the art heterogeneous silicon/III-V lasers, some of which will be presented in this tutorial, have exceeded the best of the monolithic III-V lasers in some aspects, such as laser linewidth and tuning range.

The outline of this tutorial is as follows: In Sec. II, we provide a formal definition of laser phase noise and spectral linewidth as

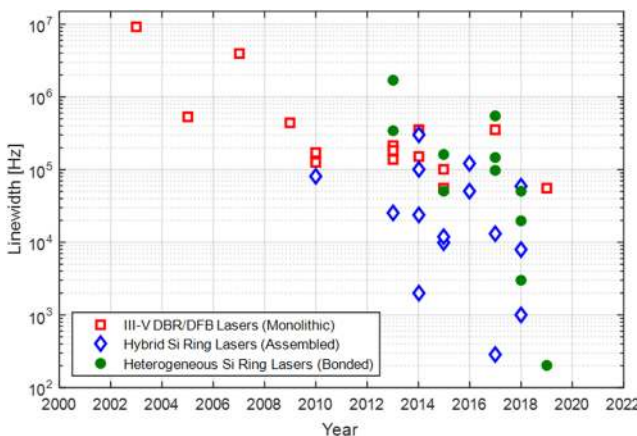


FIG. 3. Progress in Lorentzian linewidth of semiconductor lasers over the past two decades. While monolithic lasers have not improved beyond 50 kHz or so, hybrid and heterogeneous silicon lasers have pushed Lorentzian linewidths to subkilohertz levels in recent years.

used in the context of this tutorial. We discuss techniques to accurately characterize the linewidth of the laser. In Sec. III, we discuss the fundamental techniques behind linewidth reduction in lasers. We classify lasers as either solitary cavity lasers in which there is only a single section or extended cavity lasers in which there is a passive section longitudinally coupled to the gain section. We outline basic design methodology that can be used to achieve the narrow linewidth in each case. In Sec. IV, we provide some examples of heterogeneous silicon/III-V lasers that have been optimized for the narrow linewidth. We discuss distributed feedback (DFB) lasers, narrowly tunable distributed Bragg reflector (DBR) lasers, as well as widely tunable ring resonator-based lasers. The design methodologies covered in Sec. III are applied to each type of laser, and results are shown. Finally, we identify areas in which further improvements are needed in Sec. V. We investigate techniques at the system level such as laser stabilization, as well as exploratory concepts that can improve the laser at the device level.

II. FREQUENCY NOISE AND SPECTRAL LINEWIDTH OF SEMICONDUCTOR LASERS

This section provides readers with a brief summary on some technical terms and measurement methods commonly used to characterize and benchmark the laser noise and spectral purity. In Sec. II A, we discuss the link between frequency noise characteristics of the laser to its spectral line shape and linewidth. In Sec. II B, we discuss measurement methods for precise laser noise/linewidth characterization. Within the scope of this paper, lasers are single frequency.

A. Basics of frequency noise and spectral line shape

Below the relaxation oscillation frequency, the frequency noise spectrum of a free-running semiconductor diode laser typically features two distinct frequency ranges with different characteristics. At the lower frequency range, the noise spectrum is dominated by various $1/f$ noises which decay with frequency following $1/f^\alpha$ with $\alpha > 0$, as shown in Fig. 4(a). Other kinds of “technical noises” that originate from sources external to the laser could also meddle in the low frequency range. At higher frequencies where the $1/f$ noises and other technical noise die out, the white noise caused by the random processes of spontaneous emission and carrier fluctuations becomes dominant.

The laser optical field power spectral density, or laser “spectral line shape,” can directly be found from the laser frequency noise by integrating over the full range of Fourier frequency,^{63,64} as given in Eq. (1), where ν_0 is the laser’s center optical frequency, $S_E(\nu)$ is the optical power spectrum density (PSD) at optical frequency ν , E_0 is the amplitude of optical field (assumed to be constant as amplitude noise is neglected), and $S_\nu(f)$ is the frequency noise PSD at the Fourier frequency f ,

$$S_E(\nu) = E_0^2 \int_0^\infty \cos[2\pi(\nu - \nu_0)\tau] \times \exp\left[-4 \int_0^\infty S_\nu(f) \frac{\sin^2(\pi f \tau)}{f^2} df\right] d\tau. \quad (1)$$

Although not analytically solvable in general cases, it has been shown that the typical spectral shape of a laser is dominantly determined

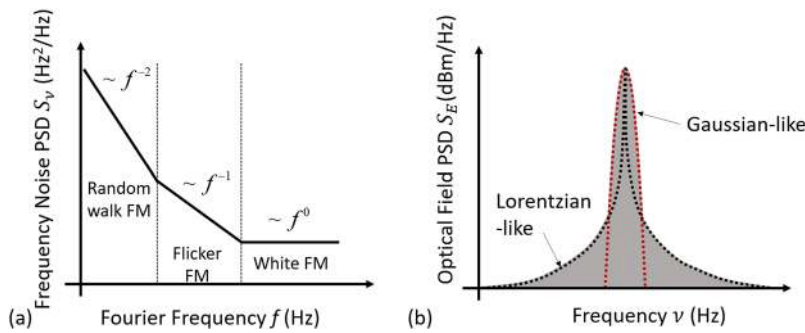


FIG. 4. Illustrative frequency noise spectrum and line shape of a single frequency laser: (a) typical frequency noise power spectral density (PSD) of a laser, where $1/f^\alpha$ noises [e.g., random walk frequency modulation (FM) noise and flicker FM noise] dominate in the low frequency range and quantum-limited white FM noise prevails in the high frequency range. Both axes are drawn in logarithmic scale. (b) The corresponding spectral line shape of the laser optical field shows Gaussian-like behavior near the peak and Lorentzian-like behavior on the wings. Both axes are drawn in linear scale.

by the noise in the low frequency range, while the noise in the high frequency range contributes to the wings (or tails).⁶⁵ Therefore, the laser spectral profile can be approximated as a combination of Gaussian-like shape (contributed by the $1/f$ noise) near the center of the line shape and Lorentzian-like shape (contributed by the quantum-limited white noises) near the tails of the spectrum, as illustrated in Fig. 4(b), or equivalently a Voigt profile.⁶⁴

In the absence of $1/f$ noise, we can see that the spectrum of the laser obtains a Lorentzian line shape by putting $S_v(f) = S_v^0$ (constant) in Eq. (1). The linewidth of this Lorentzian spectrum, equal to πS_v^0 , sets the minimum achievable linewidth of the laser when it is subjected solely to the white quantum-noise processes. Thus, the “Lorentzian linewidth” is referred to as “fundamental linewidth,” “intrinsic linewidth,” or “instantaneous linewidth.” It is also widely called “Schawlow-Townes linewidth” as its theoretical formula was first given by Schawlow and Townes in their famous paper.⁶⁶

Due to the aforementioned reasons, the “integrated linewidth”—defined as the full-width-half-maximum (FWHM) of the optical field power spectral density profile—is primarily representative for noise in the low frequency range only. This linewidth is important in spectrometry, metrology, or sensing. On the other hand, for high speed applications such as in data communications, the laser noise characteristics at high frequencies is of more importance because that noise region contributes mainly to phase-error variance of coherent communication links.^{67,68} In such cases, the Lorentzian linewidth is more applicable. The target subject discussed in this tutorial is the Lorentzian linewidth. Electrical feedback and locking techniques have been very effective in linewidth reduction at low frequencies, but it is challenging for those techniques to be effective at the high frequency range due to bandwidth limitations. Therefore, it is necessary to obtain low intrinsic noise in free running lasers.

B. Laser frequency noise and linewidth characterization

Since first introduced in 1980,⁶⁹ the delayed self-heterodyne interferometer (DSHI) is perhaps the most widely used among all

the laser spectral linewidth characterization methods, mainly due to its simplicity. A schematic of the measurement setup is shown in Fig. 5. Details of the measurement principle can be found in many references elsewhere.^{69,70} The profile of the heterodyned spectrum is given in Eq. (2), where τ_d is the delay time between the two arms of the unbalanced Mach-Zehnder Interferometer (MZI),

$$S_E(\nu) = E_0^2 \int_0^\infty \cos[2\pi(\nu - \nu_0)\tau] \times \exp\left[-4 \int_0^\infty S_v(f) \frac{\sin^2(\pi f \tau)}{f^2} \sin^2(\pi f \tau_d) df\right] d\tau. \quad (2)$$

Despite being widely used, the DSHI technique has some limitations. First, the length of delay may be prohibitively long as it must be larger than the coherence length of the laser. Second, it should be noted that the heterodyned interferometer basically acts as a sampling filter on the integrals of frequency noise due to the term $\sin^2(\pi f \tau_d)$ inside the integrals in Eq. (2). This term also effectively cuts off the frequency noise region below $\sim 1/\tau_d$. Thus, the integrated linewidth measured with the DSHI technique is influenced by the choice of the delay length parameter.⁷¹ Third, due to the slow measurement and large delay length, the measured spectrum is highly susceptible to many technical noises from the surrounding environment. This might cause drifting of the spectra leading to distorted profiles.⁷² One usually has to fit the tails of the measured spectrum (at least -20 dB down from the peak) to approximate the Lorentzian linewidth of the laser since the central part near the peak of the spectral line shape is masked by $1/f$ noise and technical noise in the low frequency range. The limited signal to noise ratio makes it challenging to achieve an accurate estimation.

A more advanced measurement technique to characterize the linewidth is a direct frequency noise measurement using a frequency discriminating scheme, as shown schematically in Fig. 6. Using a frequency discriminator, such as an unbalanced MZI with sub-coherent delay difference, the fluctuations of laser frequency is converted to fluctuations of interferometer output amplitude recorded

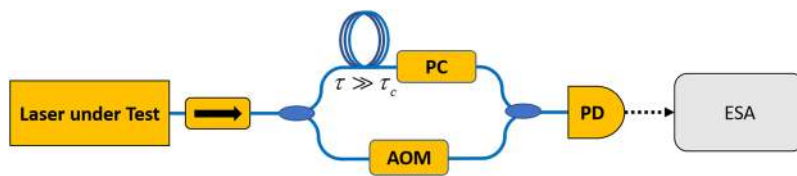


FIG. 5. Delayed self-heterodyne setup (the AOM included) or homodyne setup (the AOM excluded) to measure the laser spectral line shape. Term definitions—PC: polarization controller; AOM: acousto-optic modulator; PD: photodiode; ESA: electrical signal analyzer.

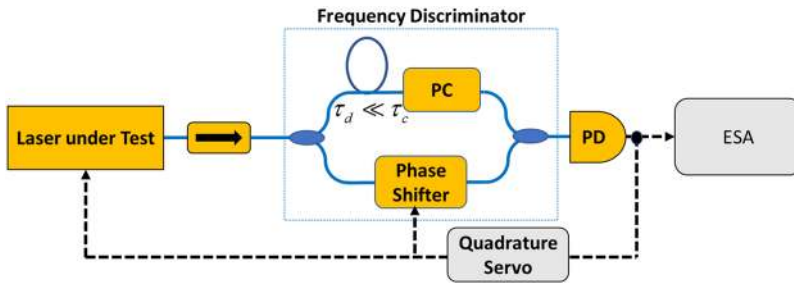


FIG. 6. Laser frequency noise measurement using a frequency discriminator which is an unbalanced Mach-Zehnder interferometer as an example.⁷³ The electrical servo is used to control either the phase-shifter or the laser to maintain the quadrature biasing for optimal sensitivity. Term definitions—PC: polarization controller; PD: photodiode; ESA: electrical signal analyzer.

by a photodiode. The time-domain data from the photodiode can then be processed to obtain the frequency (or phase) power spectral density of the lasers. A control servo needs to be implemented to control either the laser or the phase shifter to keep the bias point at quadrature for maximal sensitivity. Although the system is more complex, it allows one to observe the full noise characteristics of the lasers.

Once one has the frequency noise spectrum of the lasers, it is straight forward to accurately acquire the quantum limited Lorentzian linewidth, as given by Eq. (3), where S_v^0 is the single-sided PSD of the white frequency noise,

$$\Delta\nu_{\text{Lorentzian}} = \pi S_v^0. \quad (3)$$

It is, in principle, possible to construct the optical field PSD from the frequency noise measurement using Eq. (1) and then calculate the FWHM to determine the integrated linewidth of the laser. However, to avoid that cumbersome procedure, an effective integrated (or also *integral*) linewidth $\Delta\nu_{\text{int}}$ can be approximated to be the Fourier frequency at which the phase modulation index equals unity.⁷⁴ In other words, $\Delta\nu_{\text{int}}$ is found by solving Eq. (4), where $S_\varphi(f) = \frac{S_v(f)}{f^2}$ is the expression for the phase noise PSD,

$$\int_{\Delta\nu_{\text{int}}}^{\infty} S_\varphi(f) df = \int_{\Delta\nu_{\text{int}}}^{\infty} \frac{S_v(f)}{f^2} df = \frac{1}{\pi} \text{rad}^2. \quad (4)$$

III. PRINCIPLES OF QUANTUM NOISE REDUCTION IN SEMICONDUCTOR LASERS

Quantum noise in semiconductor lasers originates from spontaneous emission via two processes. One ($\Delta\nu_\varphi$) is a direct process in which the phase fluctuation is directly caused by spontaneous emitted photon fields adding to the lasing photon field. The other process ($\Delta\nu_N$) is an indirect result of spontaneous emission: generation of spontaneous emitted photons causes photon density fluctuation in the cavity, causing the carrier density to change (through a stabilizing relaxation oscillation to restore the carrier-photon steady state), which in turn leads to the change in the refractive index and results in lasing frequency fluctuation.^{75,76} Since the second process takes as much time as oscillation relaxation needs, it only contributes to the laser noise within the frequency range below the relaxation oscillation frequency. Combining both processes, the modified Schawlow-Townes-Henry equation for the Lorentzian linewidth is obtained^{70,75} and shown in the following equation:

$$\Delta\nu = \underbrace{\frac{R_{sp}}{4\pi n_p}}_{\Delta\nu_\varphi} + \underbrace{\frac{R_{sp}}{4\pi n_p} \alpha_H^2}_{\Delta\nu_N} = \frac{R_{sp}}{4\pi n_p} (1 + \alpha_H^2). \quad (5)$$

In Eq. (5), α_H (unitless) is the linewidth enhancement factor, a material-dependent parameter that represents the relationship between the imaginary and real parts of the refractive index. It has a nonzero value in most semiconductor materials due to their non-symmetrical gain spectra.⁷⁷ R_{sp} (s^{-1}) is the spontaneous emission rate coupling to the lasing mode, and n_p is the total number of photons stored in the cavity. To make this equation better connected with physical cavity design parameters, we rewrite this equation as Eq. (6), where h is Planck's constant, ν is the laser frequency (Hz), n_{sp} is the population inversion factor, P is the total emitted power out of the cavity (W), and Q (Q_E) is the loaded (external) quality factor of the laser cold cavity. The derivation is given in Subsection 2 of the Appendix,

$$\Delta\nu = \frac{\pi h \nu^3 n_{sp}}{P Q_E Q} (1 + \alpha_H^2). \quad (6)$$

The *intrinsic (internal) quality factor* is the limitation of a given cavity that is isolated from any variable loading due to mirrors or resonator coupling. Thus, Q_I is determined by the cavity's internal loss, averaging over all the losses in active (α_a) and passive (α_p) regions,

$$Q_I^{-1} = \frac{\langle \alpha_i \rangle \lambda}{2\pi n_g} = \frac{\langle \alpha_a \rangle V_{\text{active}} + \langle \alpha_p \rangle V_{\text{passive}}}{V_{\text{total}}} \frac{\lambda}{2\pi n_g}. \quad (7)$$

The *external quality factor*, on the other hand, accounts for the loss due to the total power out-coupling ratio (κ^2) (and excess loss due to imperfect coupling schemes, which is neglected here) distributed over the cavity length. In laser physics, this is commonly represented by the term mirror loss α_m , as expressed in the following equation:

$$Q_E^{-1} = \frac{\ln\left(\frac{1}{1-\kappa^2}\right)}{L} \frac{\lambda}{2\pi n_g} = \frac{\alpha_m \lambda}{2\pi n_g}. \quad (8)$$

Once the resonator is coupled to the outside world by a coupling scheme, the *loaded quality factor* accounts for both loss mechanisms in the cold cavity,

$$Q^{-1} = Q_I^{-1} + Q_E^{-1} = \frac{(\langle \alpha_i \rangle + \alpha_m) \lambda}{2\pi n_g}. \quad (9)$$

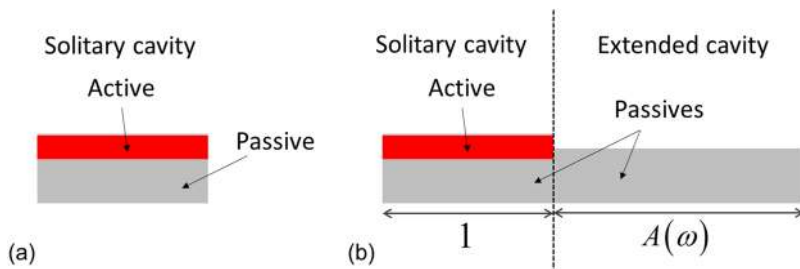


FIG. 7. Illustrative schematic of (a) a solitary cavity laser structure and (b) an extended cavity laser structure.

The strategy for designing the narrow linewidth laser becomes clear from Eqs. (6)–(9): increasing the quality factors Q s of the cold cavity. As suggested by Eq. (7), a high intrinsic Q_I calls for low internal loss of the cavity. Dominant contributions to the internal loss in a laser cavity can be distributed to absorption losses in the laser active regions, and absorption and scattering loss in the passive sections. As the absorption loss from the active region is unavoidable in the gain material, cavity designing should focus on:

- (1) reduction of the loss in the passive region and
- (2) increase in the ratio between the optical mode volume in low loss passive with respect to the mode volume in the active region.

On the other hand, a low (distributed) mirror loss is required for obtaining a high external Q_E , as shown in Eq. (8). That comes down to two design parameters:

- (3) increase in cavity length and
- (4) decrease in out-coupling ratio κ^2 , although one should note that a too low κ^2 would hurt the differential efficiency of the laser output power.

Next, we discuss the implementation of these four “recipes” to achieve low noise performance in heterogeneously integrated lasers, categorized into two types based on the structures of their cavity: solitary cavity lasers [Fig. 7(a)] and extended cavity lasers [Fig. 7(b)]. In solitary cavity lasers, the active and passive regions share the same longitudinal space; hence, at any point in the cavity the optical mode always sees both active and passive media. Extended cavity lasers are formed by coupling an additional passive section to a solitary section with a negligible reflection at the interface between the two.

A. Solitary cavity low noise laser design

Si/III-V heterogeneous lasers differentiate themselves from conventional semiconductor lasers by the silicon waveguide being an integral part of the optical mode. Since the silicon layer is undoped as the carriers only flow through the III-V layers, a low optical loss in the silicon is achievable.⁷⁸ Furthermore, by simply lowering the physical volume of the active layer (e.g., a number of quantum-well layers) and optimizing the geometry of the silicon waveguides, it is possible to achieve a high confinement factor of the optical mode in silicon. In other words, the first two noise reduction strategies (1) and (2) are greatly suitable to be utilized in designing low noise Si/III-V heterogeneous lasers. Specific examples of such structures are provided in Sec. IV A.

B. Extended (external) cavity low noise laser design

Extended cavity lasers bring in an additional low loss passive structure, simultaneously gaining in linewidth reduction via recipes (1) and (2). Having a cavity comprising both active and passive in the longitudinal direction also means that the laser total cavity length is extended—satisfying recipe (3). That ultimately increases both internal Q_I [via Eq. (7)] and external Q_E [via Eq. (8)]. There are various types of extended passive cavities, e.g., single-frequency Bragg gratings, sampled-gratings, and ring resonators, or a combination of rings and gratings. They can involve coupling to another waveguide such as an ultralow loss silicon nitride waveguide.⁶² In all cases, the external cavity possesses a strong wavelength dispersion to provide sufficient mode filtering required for single mode lasing. This dispersive property, interestingly, brings about another noise reduction effect beyond what was captured in Eqs. (5)–(9)—the detuned loading or optical negative feedback effect.

To see this in the most comprehensive way, we follow the formalism first carried out by Patzak *et al.* in Ref. 79, Kazarinov and Henry in Ref. 80, and Vahala and Yariv in Ref. 81. Our extended cavity lasers can be modeled as a three-section laser shown in Fig. 8(a). Following the effective mirror model, the laser is simplified in Fig. 8(b). Here, the gain section (formed by the heterogeneous Si/III-V waveguide) and the front mirror can be lumped into a single active section on the left-hand-side with the reflection coefficient r_1 . The phase section and all waveguides used for routing are lumped into the passive section, connecting to the ring mirror on the right-hand-side. The reflection on the active-passive transition is neglected in the analysis.

We can replace all the extended cavity parts of the laser by an effective mirror with complex wavelength dependence represented by $r_{eff}(\omega)$. This substitution is valid since we are looking for steady-state solutions in this analysis.⁷⁰ The effective reflectivity is the

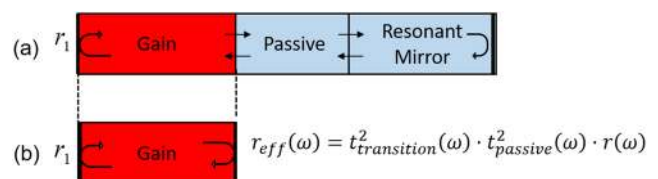


FIG. 8. Modeling of the diode laser with a resonant mirror as the extended cavity: (a) block diagram representation of the laser sections and (b) equivalent cavity with the effective mirror to model the extended cavity.

product of transfer functions of all passive parts and the active-passive transition, given by the following equation:

$$r_{\text{eff}}(\omega) = t_{\text{transition}}^2(\omega) \cdot t_{\text{passive}}^2(\omega) \cdot r(\omega). \quad (10)$$

Here, $t_{\text{transition}}(\omega)$ is simply an attenuation constant representing the transmission loss at the active-passive transition. For a total length L_p accounted for all passive waveguide routing and phase section, the transfer function for the passive waveguides is given by $t_{\text{passive}}(\omega) = \exp(-\alpha_p L_p - j\beta_p L_p)$, where α_p and β_p are the waveguide electric field propagation loss and the effective propagation constant in the passive waveguides, respectively. The last term $r(\omega)$ expresses the frequency dependence of the extended cavity reflectivity. The effective mirror term $r_{\text{eff}}(\omega)$ can be separated into effective amplitude and phase parts as $r_{\text{eff}}(\omega) = |r_{\text{eff}}(\omega)|\exp(-j\varphi(\omega))$. The real part, amplitude factor $r_0(\omega)$, represents the field feedback from the extended passive section to the gain section; $\tau_0 = \frac{2n_g L_a}{c}$ is the photon round-trip time in the active section. The linewidth of the extended cavity laser can then be calculated by Eq. (11), where $\Delta\nu_0$ represents the Lorentzian linewidth of a solitary Fabry-Perot diode laser with mirror reflectivities r_1 and $|r_{\text{eff}}(\omega)|$,

$$\Delta\nu = \Delta\nu_0 \frac{1}{\left(1 + \frac{\alpha_H}{\tau_0} \frac{d \ln |r_{\text{eff}}(\omega)|}{d\omega} + \frac{1}{\tau_0} \frac{d\varphi_{\text{eff}}}{d\omega}\right)^2}. \quad (11)$$

As output power P from the laser is collected on the low reflective side (r_1), the equation for $\Delta\nu_0$ is given by Eq. (12), where v_g is the group effective index, h is the Planck constant, ν is the lasing frequency, n_{sp} is the spontaneous emission factor, $\alpha_{\text{tot}} = \alpha_i + \alpha_m$ is the total loss, $\alpha_m = -\frac{1}{L_a} \ln(r_1 |r_{\text{eff}}(\omega)|)$ is the mirror loss, and α_i is the internal loss of the active section,

$$\Delta\nu_0 = \frac{1}{4\pi} \frac{v_g h \nu n_{\text{sp}} \alpha_{\text{tot}} \alpha_m}{P \left[1 + \frac{r_1}{|r_{\text{eff}}(\omega)|} \frac{1 - |r_{\text{eff}}(\omega)|^2}{1 - r_1^2}\right]} (1 + \alpha_H^2). \quad (12)$$

In other words, due to the frequency dependence of the phase and reflectivity of the extended cavity, the linewidth of the otherwise solitary Fabry-Perot laser is reduced by a factor of $F^2 = (1 + A + B)^2$, where $A(\omega) = \frac{d\varphi_{\text{eff}}(\omega)}{d\omega}$ and $B(\omega) = \frac{\alpha_H}{\tau_0} \frac{d \ln |r_{\text{eff}}(\omega)|}{d\omega}$.

It is clear that the factor $A(\omega)$ reflects the increase in roundtrip accumulated phase—equivalent to the effective cavity length enhancement provided by the extended cavity. An increase in the factor A basically means that the passive length of the laser cavity becomes longer, and therefore the laser linewidth is narrowed due to recipes (2) and (3).

The meaning of factor $B(\omega)$ is more subtle and unique to a semiconductor extended cavity laser. It represents the magnitude of the optical negative feedback effect⁸⁰ (also known as detuned loading⁸¹) that helps stabilize the laser frequency via the phase-amplitude coupling of the lasing field—a phenomenon associated with the linewidth enhancement factor α_H , as illustrated in Fig. 9, where the mirror reflectivity is a resonant function of the optical frequency. When the lasing frequency is at the marked point (i.e., the positive slope side), an increase in laser frequency increases the reflectivity, leads to the increase in the photon density in the cavity,

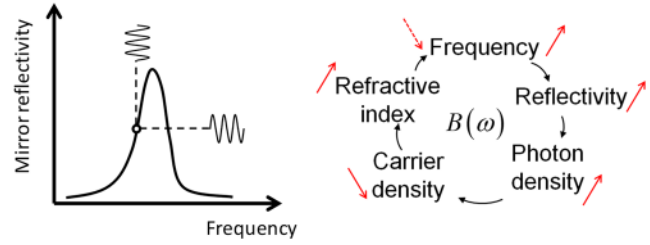


FIG. 9. Illustrative explanation of the detuned loading (or optical negative feedback) effect provided by a dispersive mirror.

and hence decreases carrier density, which in turn causes the frequency to decrease due to the carrier plasma effect. This negative feedback loop helps stabilize the laser frequency and hence lower the laser frequency noise. In contrast, if the lasing occurs on the other side of the mirror resonant peak (i.e., negative slope side), a positive feedback loop is formed with which frequency noise is amplified and linewidth is broadened.

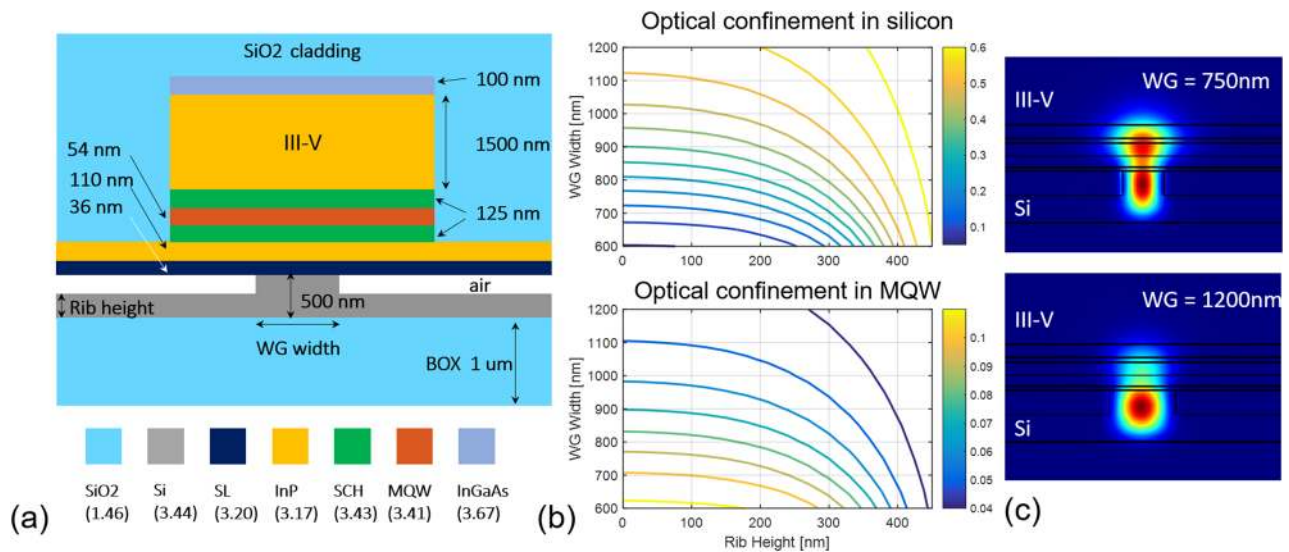
As the magnitude of the negative feedback effect depends on the strength of the coupling between carrier density and optical frequency via the carrier plasma effect, factor B is proportional to the linewidth enhancement factor α_H ,⁸² the factor that accounts for the broadening of the linewidth in solitary lasers in the first place. In other words, the detuned loading effect introduced by the frequency dispersion of the extended cavity diminishes the “linewidth enhancement” role of factor α_H in the frequency noise of the laser. This phenomenon makes α_H “harmless” or even “advantageous” for the linewidth in extended cavity lasers, that is, a significant advantage compared to solitary lasers in which the Lorentzian linewidth scales with $(1 + \alpha_H^2)$.

IV. HETEROGENEOUSLY INTEGRATED LASER DEMONSTRATIONS FOR LOW NOISE

In this section, we provide some practical examples of heterogeneous silicon/III-V lasers that have been designed for the narrow linewidth. We first explore single wavelength lasers such as DFB and DBR structures and then move onto widely tunable ring resonator-based lasers.

A. DFB lasers

Due to its simplicity, DFB lasers arguably are the workhorse of semiconductor lasers when considering practical applications. In the heterogeneous silicon/III-V platform, the DFB gratings can be defined in silicon, by either etching the surface of the waveguide or creating sidewall corrugations, prior to bonding. This alleviates the need for regrowth procedures commonly used for monolithic III-V DFB lasers. As extensively discussed in Sec. III, the key to reduce the linewidth in a DFB laser is increasing the cavity quality factors through a combination of lowering confinement factor in the active quantum wells and decreasing waveguide loss. Compared with doped III-V cladding and III-V waveguide layers typically used in conventional all III-V lasers, the undoped silicon waveguide can have much lower loss, enabling the heterogeneous silicon DFB laser to have a higher cold cavity quality factor. A simulation of

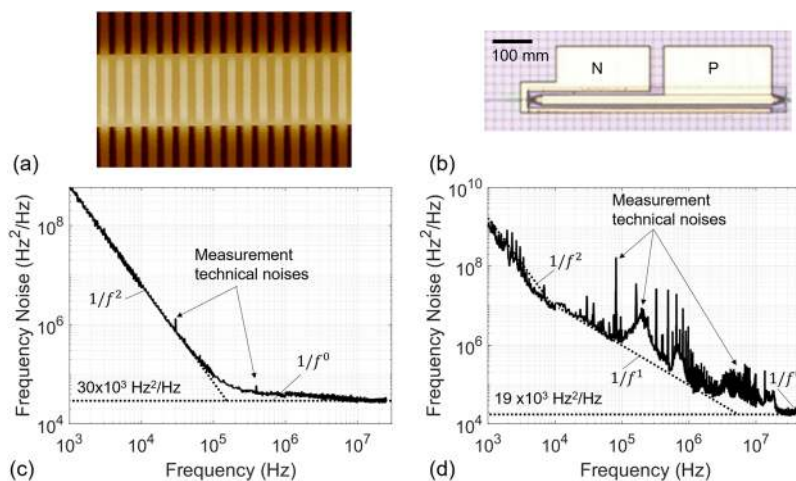


confinement factors in silicon and quantum well regions is given in Fig. 10 for varying silicon rib geometries.

Two examples of simply designed quarter-wave phase shifted DFB lasers are shown in Fig. 11. Here, the III-V gain material was directly bonded on the surface gratings on silicon waveguides to realize the laser cavity. The silicon waveguides are a standard 500 nm thick with 231 nm etch depth and a propagation loss of 1 dB/cm. On the first laser, the Si waveguide is 750 nm wide, corresponding to 31% confinement in Si and 68% in InP. The frequency noise measurement is plotted in Fig. 11(c), showing $1/f^2$ noise up to the 100 kHz frequency range, and a white noise level of 30 kHz²/Hz

dominating beyond that. The corresponding Lorentzian linewidth is extracted to be ~94 kHz. On the second one, the Si waveguide width is increased to 1.2 μm, corresponding to 57% confinement in Si and 43% in InP. Although the laser's pure frequency noise spectrum was obstructed by a lot of technical noises that we later confirmed to come from our measurement setup, it is still quite clear that the white noise level is about 19 kHz²/Hz, resulting in a 60 kHz Lorentzian linewidth.

To further reduce the confinement factor in the high loss III-V, it is possible to introduce a spacer layer between the silicon and III-V, as illustrated in Fig. 12. The thickness of this layer, usually



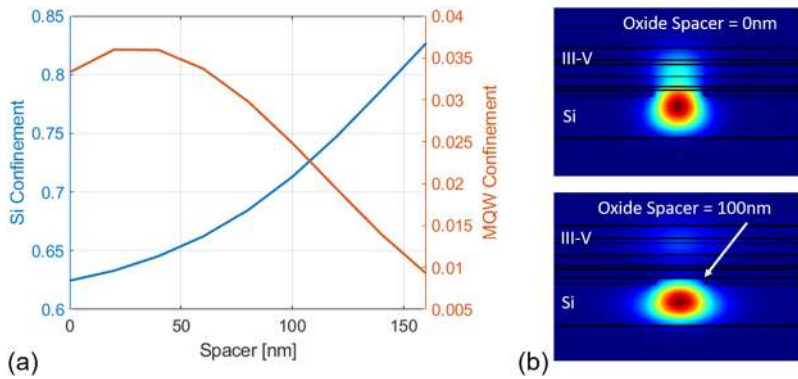


FIG. 12. (a) The addition of a spacer can also be used to further decrease silicon confinement while maintaining the hybrid silicon/III-V mode. Here, a planarized oxide spacer layer between the silicon and III-V is varied. The etch depth of silicon is assumed to be 60 nm, leaving a 440 nm tall rib waveguide. (b) The mode profile clearly shows a further increase in silicon confinement.

silica, can be precisely controlled. In Refs. ⁸³ and ⁸⁴, Santis *et al.* have used a 150 nm spacer layer combined with a high-Q resonator ($\sim 10^6$) on shallow etch silicon waveguides to form a laser cavity with quantum well confinement as low as 0.2% to significantly reduce the linewidth. The measured linewidths are as low as 1.1 kHz, with predicted values nearing 500 Hz. By nature of the high-Q cavity, these lasers have also been shown to be resilient to unintentional optical feedback,⁸⁵ making them intriguing candidates for coherent communications.⁸⁶ However, the cavity length limited to only 1 mm with the high Q design made it difficult to achieve high optical power from these devices (~ 1 mW) due to a low differential quantum efficiency. Increasing the length of the lasers should allow for improvement. To completely break this trade-off, external cavity designs are considered in Sec. IV B, which can simultaneously achieve narrow linewidth and high output power.

B. Extended DBR lasers

Heterogeneous silicon/III-V lasers allow for separate optimization of the active and passive sections of the laser and are therefore an excellent platform to realize low-noise DBRs. Traditionally, DBR lasers incorporate relatively short mirrors with fairly high kappa, in order to keep the overall cavity length of the laser short. The DBR often makes up the back mirror and is designed to be near 100% reflectivity. This does not contribute much to linewidth reduction, as shown in previously published works.^{87–89} Instead, the design mentality for a low-noise DBR laser should mimic that of ultralow

noise fiber Bragg grating lasers, in which the grating accounts for the majority of the cavity length and serves as the front mirror of the laser.^{57,90} These lasers, termed extended DBRs (E-DBRs), utilize a very long grating to simultaneously enable the narrow linewidth, while preserving stable, single mode behavior.

The elements needed to design a Bragg grating with long length and narrow bandwidths are low waveguide loss and weak index perturbations, i.e., low κ . For use in an E-DBR, the grating should be in the weak-grating limit such that the sinc approximation is accurate. In this regime, the effective length, reflectivity of the grating, and grating bandwidth (null to null across the central lobe, not FWHM) are given in Eqs. (13)–(15), respectively.⁹¹ Plots of these relevant metrics are given in Fig. 13 for a range of waveguide loss and grating lengths. From these plots, it is apparent that the overall strategy is to reduce waveguide loss as much as possible and maintain low κL over a long grating,

$$L_{\text{eff}} = \left(\frac{\tanh(\kappa L)}{2\kappa} \right), \quad (13)$$

$$R_{\text{eff}} = \tanh^2(\kappa L) \cdot e^{-2\alpha L_{\text{eff}}}, \quad (14)$$

$$\Delta\lambda_{BW} = \left(\frac{\lambda^2}{\pi n_g} \right) \sqrt{\kappa^2 + \left(\frac{\pi}{L} \right)^2}, \quad (15)$$

When considering ultralow kappas over such long gratings, the uniformity and repeatability of the grating definition must be

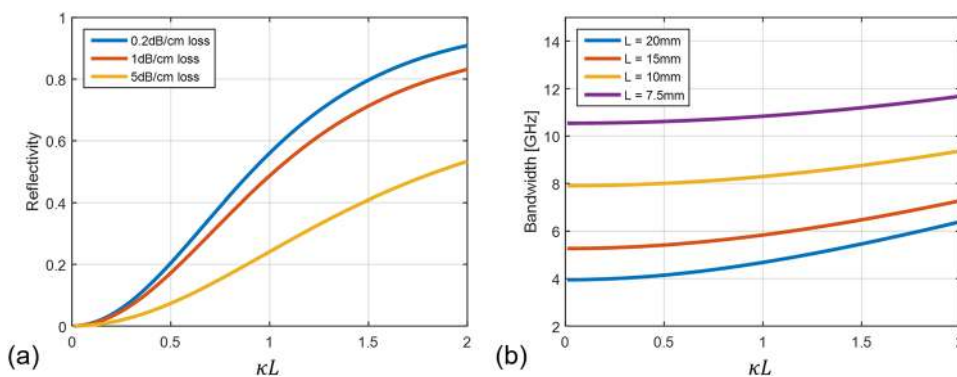


FIG. 13. Calculations of the grating (a) reflectivity and (b) bandwidth for different grating parameters. A group index of 3.8 is assumed, and the grating is assumed to be uniform.

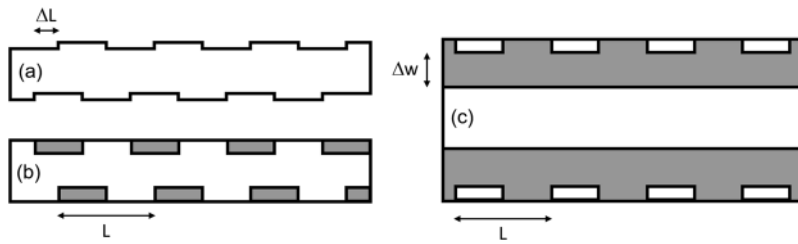


FIG. 14. Low-kappa Bragg gratings can be achieved by using an offset grating geometry where the offset (ΔL) in the (a) sidewall or (b) surface etched grating controls the strength of the grating. Alternatively, the slab of the waveguide can be modulated (c), using the offset between the grating and rib (Δw) as the control mechanism for kappa.

emphasized. For traditional sidewall or surface etched gratings, κ is directly proportional to the perturbation in waveguide width or height. As κ approaches zero, these perturbations become so small that the variance in fabrication will destroy the uniformity of the grating. Therefore, an alternate technique should be used. One way to reduce the kappa for a surface or sidewall grating without changing the perturbation strength is to misalign the perturbations on each side of the waveguide. By tuning the misalignment from zero to a half-period, the bandwidth of the grating can be precisely controlled.⁹² However, this technique may add additional loss to the waveguide over the long grating length, since the corrugations are strong. A method to controllably reduce kappa of the grating without adding significant waveguide loss is to modulate the cladding of the waveguide.^{93–95} In the case of the rib waveguide grating, periodically etched holes in the slab region can be used to provide a perturbation. For this design, κ is inversely proportional to the distance between the hole and the rib waveguide and can be controlled very precisely. Furthermore, the large separation between the holes and the waveguide preserves the low waveguide loss, making this grating an ideal design for low noise E-DBRs. Both types of gratings are depicted in Fig. 14.

Gratings are not limited to just silicon and can be extended to other waveguide platforms such as silicon nitride. Ultralow kappa gratings have been demonstrated in silicon nitride with very high performance. Compared to silicon, silicon nitride offers even lower waveguide loss, as well as a longer grating period for a given Bragg wavelength, due to its lower index. The longer grating period allows for the gratings to be patterned without resorting to e-beam lithography. For the gratings in Ref. 96, the gratings are defined in the same step as the waveguide, reducing the fabrication complexity and preserving alignment with the waveguide. For silicon, the period of the first-order grating is often at the limit of conventional

lithography without the use of immersion lithography. However, the lower index for silicon nitride is a double-edged sword as a lower group index also lowers the passive to active ratio. Therefore, the trade-offs should be carefully considered when designing a grating.

One example of a low-noise heterogeneous silicon/III-V DBR laser is shown below.⁹⁰ This laser makes use of the ultralow loss silicon platform, which is tailored for heterogeneous integration with III-V due to its matching silicon waveguide height (500 nm).⁷⁸ The laser uses a 15 mm long uniform grating section with a propagation loss of 0.16 dB/cm. The overall FWHM bandwidth of the grating is only 2.9 GHz which is narrow enough to pick out a single longitudinal cavity mode of the laser, with a reflectivity of approximately 40%. The light-current-voltage (LIV) and frequency noise measurements are shown in Fig. 15, showing a maximum output power of 37 mW on the chip, a side mode suppression ratio (SMSR) of over 55 dB, and a Lorentzian linewidth below 400 Hz.

While the E-DBR is simple to operate with only a gain section and a phase tuner, there are several disadvantages to it. It is not widely tunable, as the only real mechanism for wavelength tuning is the bias current or stage temperature, neither of which is ideal. The physical size of the laser is also long due to the length of the grating. Spiral gratings greatly reduce the footprint of the laser and also improve the uniformity of the grating as the DBR is more localized on the wafer.⁹⁷ Finally, DBR lasers are known to have mode hops, which is usually caused by thermal induced detuning between the Bragg wavelength and the cavity modes. This stems from the active and passive sections having different dn/dT . In some cases, the laser can enter a multimode state, a chaotic state, or even a mode-locked state.^{98,99} For most practical applications, the bias current is fixed and mode hops can be mitigated by active tuning of the phase section using a monitor photodiode to maximize power,

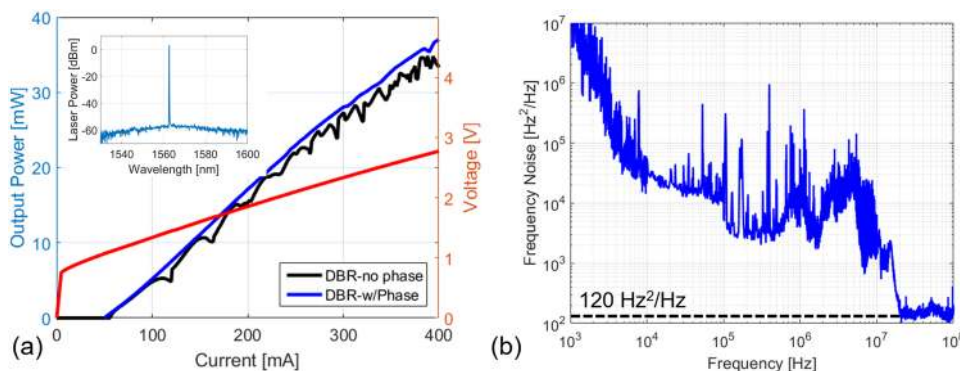


FIG. 15. (a) LIV and spectra of the E-DBR in Ref. 91. The laser consists of a 15 mm long extended Bragg grating. The laser has a phase section that can be actively tuned to avoid mode hops during the LIV sweep. (b) The laser displays a white noise level at 120 Hz²/Hz.

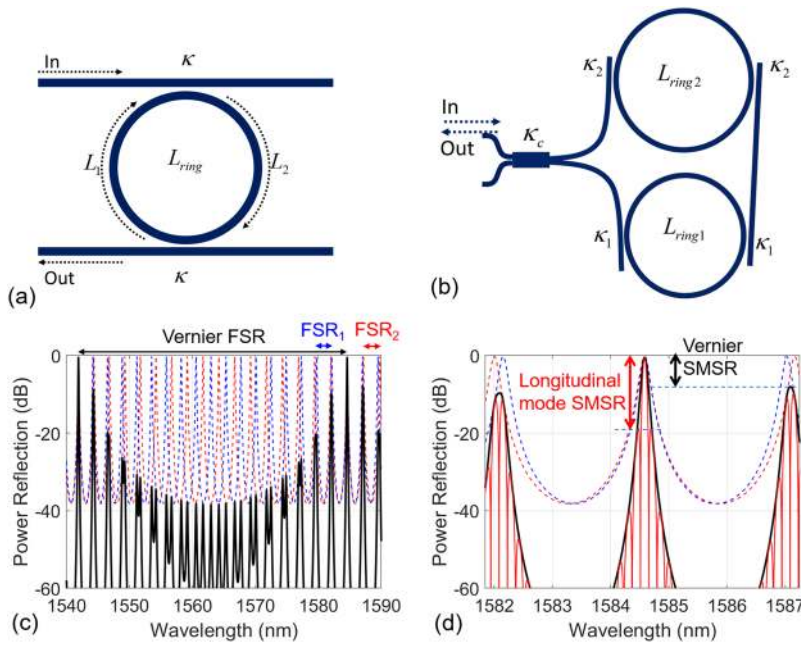


FIG. 16. (a) Schematic of an add-drop ring resonator with symmetric coupling ratios κ , ring circumference L_{ring} , and ring partial circumferences L_1, L_2 . (b) Schematic of the dual-ring mirror with coupling ratios κ_1, κ_2 and circumferences L_{ring1}, L_{ring2} formed in loop with a coupler with coupling ratio κ_c . (c) Schematic reflection spectra of the dual-ring mirror (black curve) where the Vernier FSR is much larger than individual ring FSRs shown in red and blue dashed-lines. (d) Schematic of the wavelength spectrum in a dual-ring resonator laser showing longitudinal modes enveloped by Vernier modes. The close-in longitudinal mode SMSR and Vernier SMSR are illustrated.

which generally corresponds to a stable, single mode regime of operation.

C. Ring-resonator based widely tunable lasers

The ring resonator is a device that has been intensely studied as a wavelength filter in silicon photonics. The high-index contrast allows for extremely tight bend radii and very compact footprint. However, when designing ring resonators for tunable lasers, larger rings are considered, as the Vernier architecture is often used in conjunction with rings to enhance the tuning range of the laser. For a typical tuning range spanning 40 nm, a single ring would need to have a radius on the order of $1\ \mu\text{m}$ to have a large enough free spectral range (FSR) [as shown in Eq. (16), where n_g is the group index, λ is the wavelength, and L_{ring} is the circumference of the ring]. If two rings are used as shown in Fig. 16, the tuning range can be extended significantly by the expression of Vernier FSR in Eq. (17),

$$FSR_m = \frac{\lambda^2}{n_g \cdot L_{ring\ m}}, \quad (16)$$

$$FSR_{Vernier} = \frac{FSR_1 \cdot FSR_2}{|FSR_1 - FSR_2|}. \quad (17)$$

One of the widely used Vernier structures is the multiring mirror, where add-drop configured ring resonators in Fig. 16(a) are cascaded in series within a loop mirror formed with a 2×2 or 1×2 coupler in Fig. 16(b). The optical spectrum of the dual-ring Vernier mirror is overlaid with the individual ring spectra in Fig. 16(c), showing the difference between the Vernier FSR vs individual ring FSR. Once operating as laser's extended cavity, the determination and stability of the lasing mode is influenced by both Vernier mode side mode suppression ratio (SMSR) and longitudinal close-in mode SMSR, as depicted in Fig. 16(d). High SMSRs are crucial for stable single frequency operation of the lasers.

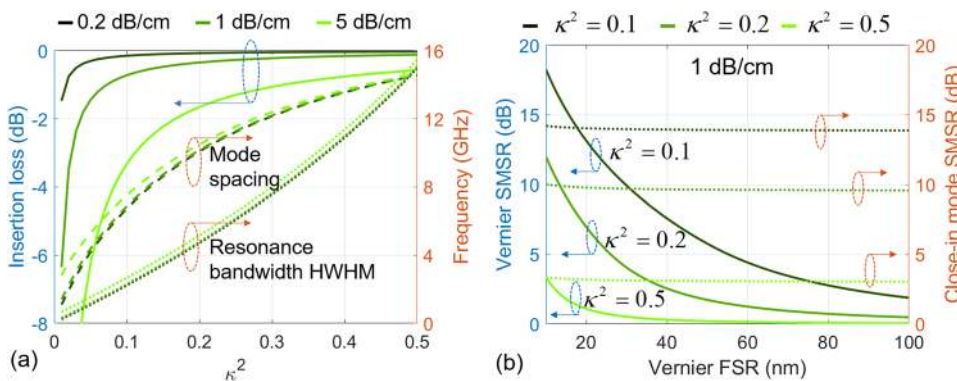


FIG. 17. (a) Trade-off between the reflection resonance bandwidth (HWHM) vs the longitudinal mode spacing and the total ring resonator insertion loss. (b) Trade-off between wavelength tuning range (determined by the Vernier FSR of the ring-resonator mirror) and the SMSR of the optical modes at 3 values of coupling ratio and waveguide loss of 1 dB/cm.

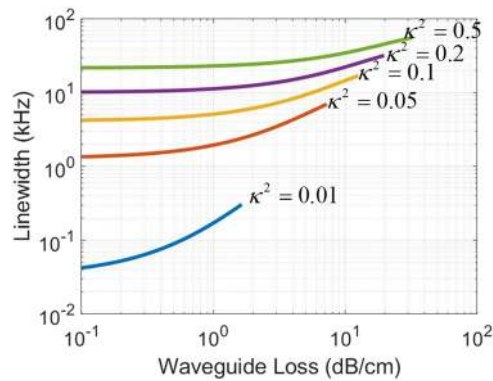


FIG. 18. Laser linewidth as a function of wavelength loss at varying power coupling ratio κ^2 for a dual-ring Vernier laser.

In addition to being easily tunable, ring resonators have the added benefit of enhanced optical length at resonance. Unlike gratings, the effective length through a ring resonator exceeds the physical length, which means that the footprint needed to achieve a similar effective length is greatly reduced. The effective length through a resonator is maximized at resonance, as given in Eq. (18), although it has been pointed out in Sec. III that the resonance may not be the optimal point of operation in terms of linewidth due to the detuned loading effect,

$$L_{\text{eff}} = \left(\frac{L_2}{L_{\text{ring}}} + \frac{1 - \kappa^2}{\kappa^2} \right) L_{\text{ring}}. \quad (18)$$

When designing a laser with rings as the external cavity, there is a trade-off between insertion loss and bandwidth of the filter. Having

too low of a κ means that too much power is lost as the light circulates through the ring, while having too high of a κ means that the ability for the filter to select a single cavity mode is threatened. This trade-off is shown in Fig. 17 for several values of waveguide loss.

For a typical dual-ring Vernier laser, the achievable linewidth is shown in Fig. 18. The linewidth is a strong function of the waveguide loss and coupling constant, as expected. For typical waveguide loss of 1 dB/cm and reasonable power coupling of 10%–20% into the ring (in order to avoid excessive insertion loss through the filter), the achievable linewidth is already below 10 kHz. We provide an example of a two-ring Vernier tunable laser in Fig. 19. The laser has over 40 nm of tuning, over 10 mW of output power, and a Lorentzian linewidth of 3.5 kHz.¹⁰⁰

One property of our laser that is worth re-emphasizing here is the fact that the lowest linewidth is achieved when the lasing frequency is detuned to the low-frequency side of resonance. The highest output power is obtained when the reflectivity on the back-mirror is maximized by aligning the lasing frequency to the resonance peak of the ring mirror. A direct implication of this is that the lowest linewidth operation point does not correspond to the highest output power operation point.

This detuned loading effect has been observed as shown in Fig. 20. The lasing frequency and the frequency noise were monitored simultaneously. At a fixed pump current of 120 mA to the gain region, we first tune the two ring resonators and the phase section to obtain the maximum output power (assisted by the on-chip photodiode) so that lasing occurs at the peak of the ring mirror's reflection resonance spectrum. We then start to change power to the heater on the phase section to detune the lasing frequency from the resonance peak. As we detune the lasing frequency to the positive side (up to +1 GHz), the frequency noise of the laser rapidly increased. In contrast, as we detune to the negative side

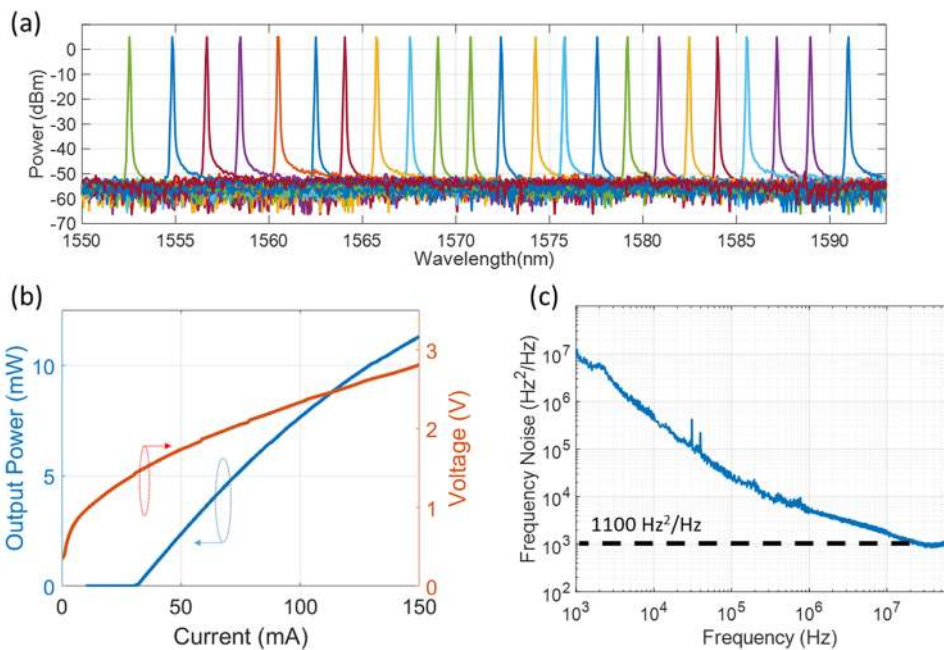


FIG. 19. (a) Coarse tuning spectra showing the tuning range of ~40 nm for the dual-ring Vernier laser. (b) L-I-V curve of the laser with a lasing wavelength of 1565 nm. (c) Frequency noise spectrum of the fabricated dual-ring Vernier laser measured at 120 mA.

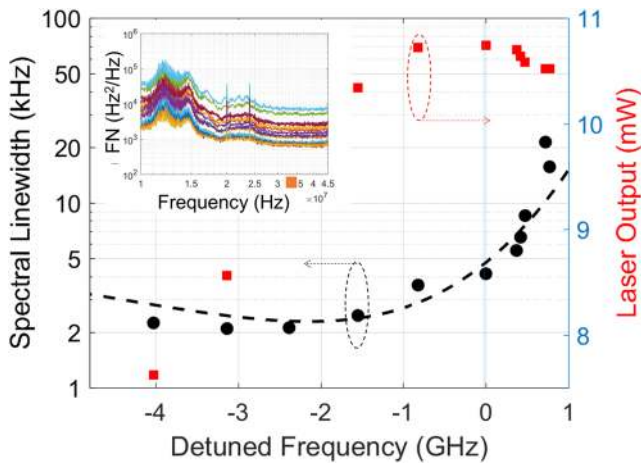


FIG. 20. Laser output power and the extracted linewidth from frequency noise measurement as functions of the detuned frequency. The dashed-line shows the theoretical curve calculated from Eq. (11). (Inset) Frequency noise spectra of the laser when detuning.

(down to -4 GHz), the frequency gradually decreases to a certain point before starting to turn back. The frequency noise spectra are plotted all together in the inset of Fig. 20. The extracted Lorentzian linewidths are plotted together with the output power as a function of the detuned frequency. The detune frequency dependence of the measured Lorentzian linewidth matches quite well with the theoretical curve (the dashed-line curve) that we calculated previously. At zero detuning, the output power of the laser is maximized, and the linewidth is about 4 kHz, about two times the minimum achievable linewidth.

In order to push the performance even further to subkilohertz levels for the two-ring Vernier laser, both waveguide loss and κ must be further reduced. However, reducing κ will come at the

cost of increased insertion loss (at a certain waveguide loss) through the filter, as shown in Fig. 18. In silicon waveguides at communication wavelengths, it also comes with increased nonlinear loss induced by two photon absorption and free carrier absorption in the high finesse (low κ) ring resonators. Therefore, an alternative solution is to increase the number of rings in the filter in order to increase the overall Q of the cavity without lowering κ too much. Three ring lasers have been previously demonstrated to have linewidth as low as 290 Hz.⁵⁸ As an example, we demonstrate the realization of low noise tunable laser with the ultrawide tuning range utilizing 4 ring resonators, as schematically shown in Fig. 21(a). The waveguide cross section in the ring mirror is based on the ultralow loss heterogeneous silicon platform and is detailed in Ref. 78. The propagation loss in silicon waveguides for these ring resonators was measured to be ~ 0.18 dB/cm. As shown in Figs. 21(b) and 21(c), a higher (>16 dB) SMSR over the whole Vernier FSR range can be achieved even with relatively high power coupling ratios ($\kappa^2 = 0.16$). With that design, the calculated FSR is about ~ 123 nm and the laser's effective cavity length was calculated to be >50 mm at resonance [Fig. 19(a)], which would provide a highly coherent laser field.

The estimated values of A , B , and F and the Lorentzian linewidth as functions of the frequency detuning from the resonance peak frequency are then calculated with the output power assumed to be 2 mW. The achievable linewidths are expected to be hundreds of Hertz, as shown in Fig. 22.

Experimental results for the fabricated quad-ring mirror laser are shown in Fig. 23. Unfortunately, due to issues with electrical contacts, the laser degraded over time, and the laser power was dropped by 10–15 dB. Despite all of those problems, the coarse tuning in Fig. 23 still shows a 120 nm wide wavelength tuning from 1484 nm to 1604 nm, which is close to the designed 123 nm Vernier FSR. The dip around the 1590 nm wavelength only appeared after laser degraded, so it is related to the degradation mechanism which is still under investigation. The 2D wavelength and corresponding SMSR map are also shown. The tuning map is a

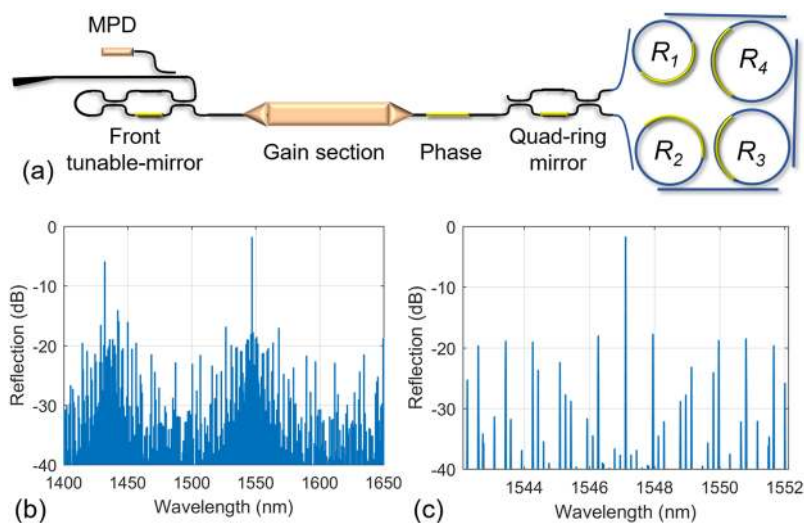


FIG. 21. (a) Schematic of a quad-ring tunable laser. (b) Broad range of a reflection spectrum of the quad-ring mirror shows the wavelength response across two Vernier FSRs. (c) Close-in spectrum shows the sidemodes near the central reflection resonance peak with SMSR >16 dB.

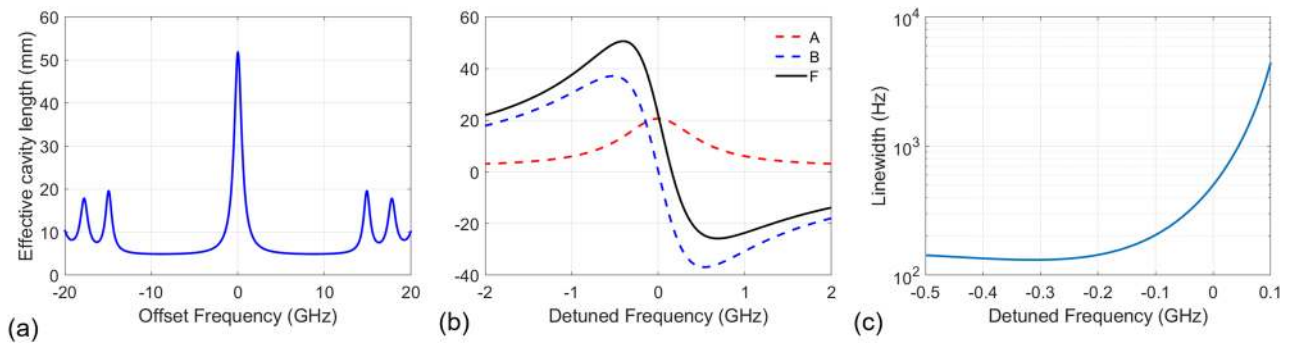


FIG. 22. (a) Calculated effective cavity length of the quad-ring mirror vs frequency offset from the resonance. (b) Calculated values for coefficients A, B, and F and (c) estimated Lorentzian linewidth as functions of frequency detuned from the reflection peak resonance for a laser output power of 2 mW.

bit erratic, partially from the additional difficulty of having one more sensitive ring that needed to be tuned and the thermal cross talk between tuning elements. A more advanced tuning mechanism might be helpful in improving the wavelength tuning performance of the laser. For example, using photoconductive heaters or in-ring detectors could provide better control.^{101,102} Care must be taken not to increase waveguide loss, or the laser performance will suffer.

The frequency noise of the quad-ring mirror laser was tested at 1565 nm wavelength and an output power of about 2 mW. The single-sided spectrum of laser frequency noise power spectral

density is shown in Fig. 24. The spectrum was somewhat hindered by the spikes at 18 MHz and harmonics, which are the frequency fringes corresponding to the free spectral range of the fiber MZI used in the measurement system. However, it is possible to observe the laser's true noise behavior outside the spike areas. We could see that the laser frequency noise is still dominated by $1/f$ noise and various external technical noises due to the nonideal measurement environment up to the 35 MHz level. A white noise level of 45 Hz²/Hz starts to be seen at about 60–80 MHz frequency range. That corresponds to a Lorentzian linewidth of 140 Hz, which is in good agreement with our calculation.

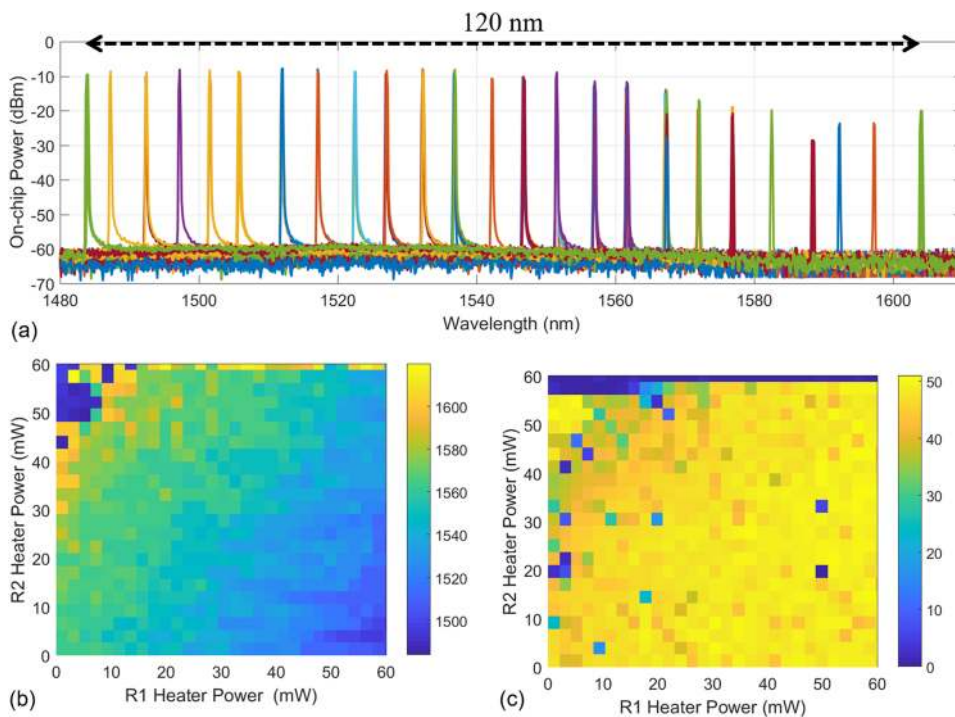


FIG. 23. Tuning characteristic of the fabricated quad-ring mirror laser. (a) Coarse tuning spectra showing the tuning range of 120 nm. (b) Two-dimensional wavelength tuning map of the dual-ring mirror laser. (c) Side-mode suppression ratio (SMSR) of the corresponding wavelength tuning map.

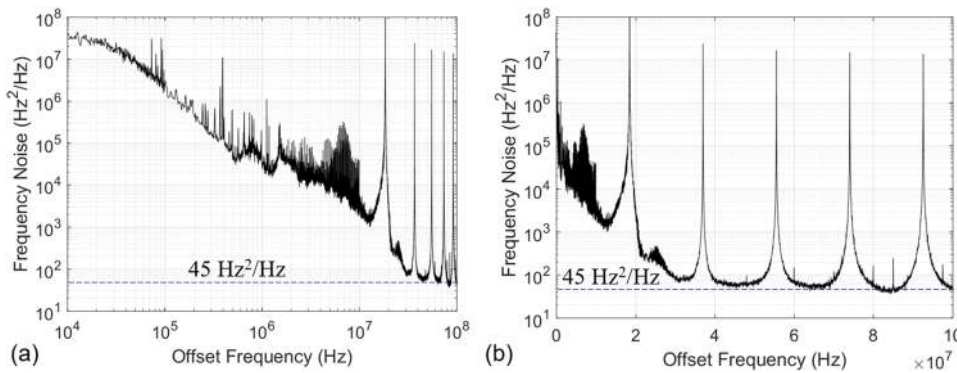


FIG. 24. (a) Frequency noise spectrum of the fabricated quad-ring mirror laser. (b) The same spectrum plotted with the x-axis in linear scale to zoom-in on the noise at high frequency range. The spikes at 18 MHz and harmonics are from the measurement tool. A white noise level of 45 Hz²/Hz is drawn.

V. FUTURE RESEARCH

A. Integrated linewidth reduction and laser stabilization

The designs presented in this work have substantially reduced the quantum limited white noise caused by the spontaneous emission in semiconductor lasers. Thanks to the low intrinsic linewidth, the frequency noise at frequencies of 100 MHz and above is extremely low. However, as revealed by the frequency noise measurement at the lower frequency range, the lasers are suffering from a very large $1/f$, aside from other measurement setup related technical noises. As a result, our calculated integrated linewidth is still relatively high—about 40 kHz for the dual-ring tunable laser (whose Lorentzian linewidth is ~ 3.5 kHz), as shown in Fig. 25. This is not ideal for many applications that work at relatively low speed or integrate over a relatively long-time frame such as sensing or spectroscopy. To suppress the laser noise in the low frequency range and achieve a low narrow integrated linewidth, optical locking the laser to an external high-Q cavity using techniques such as PDH method¹⁰³ or negative feedback loop is effective. While the frequency discriminator used in these techniques is typically off-chip, there have been several demonstrations of using an on-chip version in both silicon¹⁰⁴ and III-V¹⁰³ to achieve significant noise reduction.

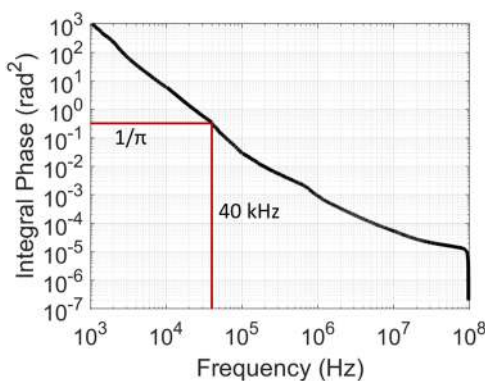


FIG. 25. Integral phase noise of the dual-ring tunable laser in Fig. 20 calculated from the measured frequency noise spectrum. An integrated linewidth (defined in Sec. II) of 40 kHz is extracted.

In general, a higher sensitivity frequency discriminator will provide greater noise reduction. For the laser in Fig. 25, an integrated linewidth of 105 Hz (equivalent to ~ 400 times reduction from free-running linewidth) was achieved by PDH locking to a high finesse Fabry-Perot silica cavity.¹⁰⁵

In addition, the laser wavelength long term stability is also important. The center wavelength of the laser is sensitive to many environmental parameters and should be stabilized in practical applications. While the details of this method are outside the scope of this tutorial, the basic principle is to stabilize any frequency fluctuations from the laser by locking to a well-known reference cavity. An error signal which details how far the center lasing frequency has drifted away from the reference frequency is fed back into a component in the laser (commonly the phase section). Both laser stabilization and locking have been demonstrated by using a high finesse Fabry-Perot silica cavity and Rb-atomic vapor cell.¹⁰⁶

B. Some exploratory directions for future heterogeneous silicon photonic lasers

As discussed in Sec. III, the linewidth enhancement factor is critical to the linewidth of a solitary laser, as the linewidth scales as $(1 + \alpha)^2$. It has been shown that quantum dots have lower α , which can even be equal to zero under optimum design.¹⁰⁷ Therefore, it is natural to expect quantum dot based solitary lasers to have lower linewidths than their quantum well counterparts. While a direct comparison is hard to make, there have been a number of quantum dot DFB lasers with less than 100 kHz linewidth.^{108,109} The same principles of linewidth reduction in this work can be carried over to a quantum dot based laser. However, the external cavity-based design does not fully enjoy the benefits of a reduction in α . This is largely due to the absence of detuned loading when the linewidth enhancement factor is small. Nevertheless, even external cavity-based lasers should see some improvement by a switch to quantum dot gain material, as one may not always operate the laser at the point of the narrowest linewidth (the highest power point could be preferred).

A second path toward improved laser performance lies in the choice of materials for the external cavity. While the majority of the devices covered in this work utilized silicon as the waveguiding material, there is room for improvement. Due to two-photon absorption, silicon waveguides do not perform as well at higher powers. One solution could be reverse biased p-n junctions to extract

the generated carriers as was done for low threshold Raman lasers. Another solution could be larger silicon waveguides such as the ultralow loss silicon waveguides⁸ or the multimicron silicon waveguide platform.¹¹⁰ The lowest loss approach is to use silicon nitride, which has losses that are as low as 0.13 dB/m in high confinement waveguides¹¹¹ and 0.045 dB/m in low confinement waveguides¹¹² with Qs of 216×10^6 demonstrated on silicon substrates.¹¹³

Another vector of improvement lies in the wavelength tuning mechanism of the ring resonator based lasers. While thermal tuning is widely used for most devices today due to its negligible optical loss, it has many drawbacks in terms of slow tuning speed, cross talk, and generally high power consumption. Methods to reduce power consumption include undercutting of silicon waveguides or use of cladding materials with higher thermal conductivity such as silicon nitride or aluminum nitride. Other exploratory directions involve moving away from thermal tuning completely. Capacitive tuning mechanisms such as MOS structures have been studied for over a decade for use in modulators.^{114,115} Recently, III-V on Si MOSCAP structures have shown high tuning efficiency with relatively low optical loss.^{116,117} As wafer bonding technology is common to both heterogeneous silicon/III-V lasers and these MOS phase tuners, they can be combined to realize tunable lasers with essentially zero tuning power consumption.³ Finally, one can envision using materials such as lithium niobate for the Pockels effect, stress-optic effect, and piezoelectric effect among others, although the integration of such materials within a laser cavity has yet to be demonstrated.

VI. CONCLUSIONS

We have explained and demonstrated some key advantages that heterogeneous integration of silicon with III-V materials provides for narrow linewidth lasers. Heterogeneous integration provides a balance of component optimization (low-loss waveguides) with process scalability (300 mm fabrication), making it an excellent platform for high-performance, narrow linewidth lasers. The concept of laser linewidth is formally defined, and the test procedures used to accurately measure laser linewidth are summarized. Techniques for linewidth reduction using external cavity design and detuned loading are discussed, and practical examples are given. The overall methodologies described here apply not only to silicon but other low-loss waveguiding platforms as well, such as silicon nitride, tantalum oxide, or lithium niobate. Low noise heterogeneous silicon/III-V DFBs, DBRs, and tunable lasers are presented. Lorentzian linewidths of the lasers are shown to be well below 1 kHz, with the potential to be below 100 Hz even for the current designs. Combined with laser locking techniques, these lasers show tremendous potential for replacing discrete lasers that are commercially used today.

ACKNOWLEDGMENTS

Research reported in this paper was performed in connection with Defense Advanced Research Projects Agency (DARPA) MTO DODOS Contract (Nos. HR0011-15-C-055 and W911NF-19-C-0003). The authors thank Paul Morton, Tin Komljenovic, Joel Guo, Chao Xiang, Jon Peters, M. J. Kennedy, and Songtao Liu for their important contributions to the results presented here.

APPENDIX: NOISE ANALYSIS AND LASER LINEWIDTH

1. Noise analysis fundamentals

We provide a very brief review on the underlying signal processing background, based on which clear definitions for all the terms related to laser noise used in the tutorial are obtained. Like any signal from an oscillator in real world, an electromagnetic wave output from a laser takes the form of an imperfect sinusoidal signal

$$v(t) = V_0(1 + \alpha(t))\cos(\omega_0 t + \varphi(t)). \quad (\text{A1})$$

In this formula, the laser oscillation is described by the $\omega_0 t$ term for phase and V_0 for amplitude, while the instantaneous phase noise and amplitude noise are represented by $\varphi(t)$ and $\alpha_0(t)$, respectively. Alternatively, one can also represent the instantaneous frequency noise term as in Eq. (A2), where the instantaneous frequency term is the derivative of the phase, $\nu(t) = \dot{\varphi}(t)$,

$$\nu(t) = V_0(1 + \alpha(t))\cos\left(\omega_0 t + 2\pi \int \nu(\tau) d\tau\right). \quad (\text{A2})$$

As represented as the functions of t , these terms are all given in the time domain. To unwrap the characteristics of the noise processes contained in the signal, we usually need to analyze the signal in the frequency domain, wherein the signal's power spectrum density (PSD) is obtained by a Fourier transformation on the autocorrelation function of the time domain signal. The (double-sided) power spectrum density of the phase and frequency noise are given by

$$S_v^H(f) = F[R(\tau)] = \int_{-\infty}^{\infty} \left(\int_{-\infty}^{\infty} v(t)v(t+\tau) dt \right) e^{-j2\pi f\tau} d\tau, \quad (\text{A3})$$

$$S_\varphi^H(f) = \int_{-\infty}^{\infty} \left(\int_{-\infty}^{\infty} \varphi(t)\varphi(t+\tau) dt \right) e^{-j2\pi f\tau} d\tau. \quad (\text{A4})$$

Note that the double-sided PSDs spread on both negative and positive frequencies. However, since all the phase and frequency signals are real signals, their PSD are even functions. The negative-frequency half-plane is therefore redundant. In practice, e.g., in most spectrum analyzers, the spectrum is effectively folded into the single-sided PSD function, as defined in the following equation:

$$S_v(f) = \begin{cases} 2S_v^H(f) & \text{for } f > 0 \\ 0 & \text{for } f < 0 \end{cases}. \quad (\text{A5})$$

As the derivation in the time domain would translate to $j\omega$ multiplication in the frequency domain, the PSDs of the frequency noise and phase noise are related by the following equation:

$$S_\varphi(f) = \frac{1}{f^2} S_v(f). \quad (\text{A6})$$

Here, the quantity unit of the frequency noise PSD $S_v(f)$ is Hz^2/Hz , while that of the phase noise PSD $S_\varphi(f)$ is rad^2/Hz .¹¹⁸

2. Laser linewidth equation derivation

Following are brief derivations to lead us from Eq. (5) to (6). Details of these derivations are found in Refs. 70 and 77. We first expand the two terms in Eq. (5), the spontaneous emission rate

coupling to the lasing mode R_{sp} and the total number of photons stored in the cavity n_p ,

$$R_{sp} = \Gamma G_m n_{sp} = \frac{\omega}{Q} n_{sp}, \quad (\text{A7})$$

$$n_p = \frac{P}{\hbar \nu} \frac{Q_E}{\omega}. \quad (\text{A8})$$

In Eq. (A7), n_{sp} is the population inversion factor and typically on the order of 1, ΓG_m is the modal gain which clamps at the modal loss $\alpha = \frac{\omega}{Q}$ when the laser lases. Here, Q is the cavity quality factor and ω is the laser's angular frequency. Equation (A8) is quite obvious as the cavity total stored power P_{store} and the emitted power P are related by $P = P_{store} \alpha_{mirror} = P_{store} \frac{Q_E}{\omega} = n_{sp} \hbar \nu = n_{sp} \frac{Q_E}{\omega}$. Now, Eq. (5) can be transformed into Eq. (6) as

$$\Delta \nu = \frac{\frac{\omega}{Q} n_{sp}}{4\pi \frac{P}{\hbar \nu} \frac{Q_E}{\omega}} (1 + \alpha_H^2) = \frac{\omega^2 \hbar \nu n_{sp}}{4\pi P Q Q_E} = \frac{\frac{1}{2\pi} \hbar \omega^3 n_{sp}}{4\pi P Q Q_E} = \pi \frac{\hbar \nu^3 n_{sp}}{P Q Q_E}. \quad (\text{A9})$$

REFERENCES

- ¹D. Thomson, A. Zilkie, J. E. Bowers, T. Komljenovic, G. T. Reed, L. Vivien, D. Marris-Morini, E. Cassan, L. Viot, J. M. Fédéli, J. M. Hartmann, J. H. Schmid, D. X. Xu, F. Boeuf, P. O'Brien, G. Z. Mashanovich, and M. Nedeljkovic, "Roadmap on silicon photonics," *J. Opt.* **18**, 073003 (2016).
- ²W. Bogaerts, P. de Heyn, T. van Vaerenbergh, K. de Vos, S. Kumar Selvaraja, T. Claes, P. Dumon, P. Bienstman, D. van Thourhout, and R. Baets, "Silicon microring resonators," *Laser Photonics Rev.* **6**, 47 (2012).
- ³D. Liang, X. Huang, G. Kurczveil, M. Fiorentino, and R. G. Beausoleil, "Integrated finely tunable microring laser on silicon," *Nat. Photonics* **10**, 719–722 (2016).
- ⁴Q. Xu, B. Schmidt, S. Pradhan, and M. Lipson, "Micrometre-scale silicon electro-optic modulator," *Nature* **435**, 325–327 (2005).
- ⁵R. A. Soref and J. P. Lorenzo, "Single-crystal silicon: A new material for 1.3 and 1.6 μm integrated-optical components," *Electron. Lett.* **21**, 953 (1985).
- ⁶R. Soref and B. Bennett, "Electrooptical effects in silicon," *IEEE J. Quantum Electron.* **23**, 123–129 (1987).
- ⁷Y. A. Vlasov, "Silicon CMOS-integrated nano-photonics for computer and data communications beyond 100G," *IEEE Commun. Mag.* **50**, s67–s72 (2012).
- ⁸T. Pinguet, S. Denton, S. Gloeckner, M. Mack, G. Masini, A. Mekis, S. Pang, M. Peterson, S. Sahni, and P. De Dobbelaere, "High-volume manufacturing platform for silicon photonics," *Proc. IEEE* **106**, 2281–2290 (2018).
- ⁹A. Rickman, "The commercialization of silicon photonics," *Nat. Photonics* **8**, 579–582 (2014).
- ¹⁰M. Suh, Q. Yang, K. Y. Yang, X. Yi, and K. J. Vahala, "Microresonator soliton dual-comb spectroscopy," *Science* **354**, 600 (2016).
- ¹¹Q.-F. Yang, B. Shen, H. Wang, M. Tran, Z. Zhang, K. Y. Yang, L. Wu, C. Bao, J. Bowers, A. Yariv, and K. Vahala, "Vernier spectrometer using counterpropagating soliton microcombs," *Science* **363**, 965–968 (2019).
- ¹²C. V. Poulton, A. Yaacobi, D. B. Cole, M. J. Byrd, M. Raval, D. Vermeulen, and M. R. Watts, "Coherent solid-state LIDAR with silicon photonic optical phased arrays," *Opt. Lett.* **42**, 4091 (2017).
- ¹³S. A. Miller, C. T. Phare, Y.-C. Chang, X. Ji, O. Jimenez, A. Mohanty, S. Roberts, M. C. Shin, B. Stern, M. Zadka, and M. Lipson, "512-element actively steered silicon phased array for low-power LIDAR," in *Conference on Lasers and Electro-Optics (OSA, 2018)*, p. JTh5C.2.
- ¹⁴J. C. Hulme, J. K. Doylend, M. J. R. Heck, J. D. Peters, M. L. Davenport, J. T. Bovington, L. A. Coldren, and J. E. Bowers, "Fully integrated hybrid silicon two dimensional beam scanner," *Opt. Express* **23**, 5861 (2015).
- ¹⁵Y. Shen, N. C. Harris, S. Skirlo, M. Prabhu, T. Baehr-Jones, M. Hochberg, X. Sun, S. Zhao, H. Larochelle, D. Englund, and M. Soljačić, "Deep learning with coherent nanophotonic circuits," *Nat. Photonics* **11**, 441–446 (2017).
- ¹⁶N. C. Harris, G. R. Steinbrecher, M. Prabhu, Y. Lahini, J. Mower, D. Bunandar, C. Chen, F. N. C. Wong, T. Baehr-Jones, M. Hochberg, S. Lloyd, and D. Englund, "Quantum transport simulations in a programmable nanophotonic processor," *Nat. Photonics* **11**, 447–452 (2017).
- ¹⁷J. Wang, S. Paesani, Y. Ding, R. Santagati, P. Skrzypczyk, A. Salavrakos, J. Tura, R. Augusiak, L. Mančinska, D. Bacco, D. Bonneau, J. W. Silverstone, Q. Gong, A. Acín, K. Rottwitt, L. K. Oxenlowe, J. L. O'Brien, A. Laing, and M. G. Thompson, "Multidimensional quantum entanglement with large-scale integrated optics," *Science* **360**, 285 (2018).
- ¹⁸D. Dai, J. Bauters, and J. E. Bowers, "Passive technologies for future large-scale photonic integrated circuits on silicon: Polarization handling, light non-reciprocity and loss reduction," *Light: Sci. Appl.* **1**, e1 (2012).
- ¹⁹D. Taillaert, P. Bienstman, and R. Baets, "Compact efficient broadband grating coupler for silicon-on-insulator waveguides," *Opt. Lett.* **29**, 2749 (2004).
- ²⁰A. Mekis, S. Gloeckner, G. Masini, A. Narasimha, T. Pinguet, S. Sahni, and P. De Dobbelaere, "A grating-coupler-enabled CMOS photonics platform," *IEEE J. Sel. Top. Quantum Electron.* **17**, 597–608 (2011).
- ²¹T. Horikawa, D. Shimura, and T. Mogami, "Low-loss silicon wire waveguides for optical integrated circuits," *MRS Commun.* **6**, 9–15 (2016).
- ²²W. Bogaerts, S. K. Selvaraja, P. Dumon, J. Brouckaert, K. De Vos, D. Van Thourhout, and R. Baets, "Silicon-on-insulator spectral filters fabricated with CMOS technology," *IEEE J. Sel. Top. Quantum Electron.* **16**, 33–44 (2010).
- ²³F. Boeuf, S. Cremer, E. Temporiti, M. Fere, M. Shaw, C. Baudot, N. Vulliet, T. Pinguet, A. Mekis, G. Masini, H. Petiton, P. Le Maitre, M. Traldi, and L. Maggi, "Silicon photonics R&D and manufacturing on 300-mm wafer platform," *J. Lightwave Technol.* **34**, 286–295 (2016).
- ²⁴"GLOBALFOUNDRIES Silicon Photonics Platform."
- ²⁵"imec's Si Photonics Platform."
- ²⁶R. Jones, P. Doussiere, J. B. Driscoll, W. Lin, H. Yu, Y. Akulova, T. Komljenovic, and J. E. Bowers, "Heterogeneously integrated InP/silicon photonics: Fabricating fully functional transceivers," *IEEE Nanotechnol. Mag.* **13**, 17–26 (2019).
- ²⁷A. Liu, L. Liao, D. Rubin, H. Nguyen, B. Ciftcioglu, Y. Chetrit, N. Izhaky, and M. Paniccia, "High-speed optical modulation based on carrier depletion in a silicon waveguide," *Opt. Express* **15**, 660 (2007).
- ²⁸G. T. Reed, G. Mashanovich, F. Y. Gardes, and D. J. Thomson, "Silicon optical modulators," *Nat. Photonics* **4**, 518–526 (2010).
- ²⁹M. N. N. Sakib, J. Sun, R. Kumar, J. Driscoll, and H. Rong, "Demonstration of a 50 Gb/s all-silicon waveguide photodetector for photonic integration," in *Conference on Lasers and Electro-Optics (OSA, 2018)*, p. JTh5A.7.
- ³⁰K. K. Mehta, J. S. Orcutt, J. M. Shainline, O. Tehar-Zahav, Z. Sternberg, R. Meade, M. A. Popović, and R. J. Ram, "Polycrystalline silicon ring resonator photodiodes in a bulk complementary metal-oxide-semiconductor process," *Opt. Lett.* **39**, 1061 (2014).
- ³¹M. Casalino, G. Coppola, R. M. De La Rue, and D. F. Logan, "State-of-the-art all-silicon sub-bandgap photodetectors at telecom and datacom wavelengths," *Laser Photonics Rev.* **10**, 895–921 (2016).
- ³²M. W. Geis, S. J. Spector, M. E. Grein, J. U. Yoon, D. M. Lennon, and T. M. Lyszczarz, "Silicon waveguide infrared photodiodes with > 35 GHz bandwidth and phototransistors with 50 AW-1 response," *Opt. Express* **17**, 5193 (2009).
- ³³J. Liu, X. Sun, R. Camacho-Aguilera, L. C. Kimerling, and J. Michel, "Ge-on-Si laser operating at room temperature," *Opt. Lett.* **35**, 679–681 (2010).
- ³⁴R. E. Camacho-Aguilera, Y. Cai, N. Patel, J. T. Bessette, M. Romagnoli, L. C. Kimerling, and J. Michel, "An electrically pumped germanium laser," *Opt. Express* **20**, 11316 (2012).
- ³⁵A. Y. Liu, S. Srinivasan, J. Norman, A. C. Gossard, and J. E. Bowers, "Quantum dot lasers for silicon photonics [Invited]," *Photonics Res.* **3**, B1 (2015).
- ³⁶D. Jung, Z. Zhang, J. Norman, R. Herrick, M. J. Kennedy, P. Patel, K. Turnlund, C. Jan, Y. Wan, A. C. Gossard, and J. E. Bowers, "Highly reliable low-threshold InAs quantum dot lasers on on-axis (001) Si with 87% injection efficiency," *ACS Photonics* **5**, 1094–1100 (2018).
- ³⁷S. Chen, W. Li, J. Wu, Q. Jiang, M. Tang, S. Shutts, S. N. Elliott, A. Sobiesierski, A. J. Seeds, I. Ross, P. M. Smowton, and H. Liu, "Electrically pumped continuous-wave III-V quantum dot lasers on silicon," *Nat. Photonics* **10**, 307–311 (2016).

- ³⁸J. C. Norman, D. Jung, Y. Wan, and J. E. Bowers, "Perspective: The future of quantum dot photonic integrated circuits," *APL Photonics* **3**, 030901 (2018).
- ³⁹A. Y. Liu and J. Bowers, "Photonic integration with epitaxial III-V on silicon," *IEEE J. Sel. Top. Quantum Electron.* **24**, 1–12 (2018).
- ⁴⁰A. Y. Liu, C. Zhang, J. Norman, A. Snyder, L. Lubyshev, J. M. Fastenau, A. W. K. Liu, A. C. Gossard, and J. E. Bowers, "High performance continuous wave 1.3 μm quantum dot lasers on silicon," *Appl. Phys. Lett.* **104**, 041104 (2014).
- ⁴¹A. W. Fang, H. Park, O. Cohen, R. Jones, M. J. Paniccia, and J. E. Bowers, "Electrically pumped hybrid AlGaInAs-silicon evanescent laser," *Opt. Express* **14**, 9203 (2006).
- ⁴²J. B. Driscoll, P. Doussi re, S. Islam, R. Narayan, W. Lin, H. Mahalingam, J. S. Park, Y. Lin, K. Nguyen, K. Roelofs, A. Dahal, R. Venables, L. Liao, R. Jones, D. Zhu, S. Priyadarshi, B. Parthasarathy, and Y. Akulova, "First 400G 8-channel CWDM silicon photonic integrated transmitter," in *IEEE 15th International Conference on Group IV Photonics (GFP), August 2018* (IEEE, 2018), pp. 1–2.
- ⁴³C. Zhang, S. Zhang, J. D. Peters, and J. E. Bowers, "8 \times 8 \times 40 Gbps fully integrated silicon photonic network on chip," *Optica* **3**, 785 (2016).
- ⁴⁴J. Hulme, M. Kennedy, R.-L. Chao, L. Liang, T. Komljenovic, J.-W. Shi, B. Szafraniec, D. Baney, and J. E. Bowers, "Fully integrated microwave frequency synthesizer on heterogeneous silicon-III/V," *Opt. Express* **25**, 2422 (2017).
- ⁴⁵Y. Zhu and L. Zhu, "Narrow-linewidth, tunable external cavity dual-band diode lasers through InP/GaAs-Si₃N₄ hybrid integration," *Opt. Express* **27**, 2354 (2019).
- ⁴⁶T. Komljenovic, M. Davenport, J. Hulme, A. Liu, C. Santis, A. Spott, S. Srinivasan, E. Stanton, C. Zhang, and J. Bowers, "Heterogeneous silicon photonic integrated circuits," *J. Lightwave Technol.* **34**, 20 (2015).
- ⁴⁷T. Komljenovic, D. Huang, P. Pintus, M. A. Tran, M. L. Davenport, and J. E. Bowers, "Photonic integrated circuits using heterogeneous integration on silicon," *Proc. IEEE* **106**, 2246–2257 (2018).
- ⁴⁸D. Huang, P. Pintus, and J. E. Bowers, "Towards heterogeneous integration of optical isolators and circulators with lasers on silicon [Invited]," *Opt. Mater. Express* **8**, 2471 (2018).
- ⁴⁹M. Pielis, J. F. Bauters, M. L. Davenport, M. J. R. Heck, and J. E. Bowers, "Low-loss silicon nitride AWG demultiplexer heterogeneously integrated with hybrid III-V/silicon photodetectors," *J. Lightwave Technol.* **32**, 817–823 (2014).
- ⁵⁰M. J. R. Heck, J. F. Bauters, M. L. Davenport, J. K. Doylend, S. Jain, G. Kurczveil, S. Srinivasan, Y. Tang, and J. E. Bowers, "Hybrid silicon photonic integrated circuit technology," *IEEE J. Sel. Top. Quantum Electron.* **19**, 6100117 (2013).
- ⁵¹T. J. Kane and R. L. Byer, "Monolithic, unidirectional single-mode Nd:YAG ring laser," *Opt. Lett.* **10**, 65 (1985).
- ⁵²"Continuous Wave Single Frequency IR Laser NPRO 125/126 Series."
- ⁵³"NP Photonics."
- ⁵⁴"Koheras AdjustiK E15."
- ⁵⁵W. Liang, V. S. Ilchenko, A. A. Savchenkov, A. B. Matsko, D. Seidel, and L. Maleki, "Whispering-gallery-mode-resonator-based ultranarrow linewidth external-cavity semiconductor laser," *Opt. Lett.* **35**, 2822 (2010).
- ⁵⁶W. Liang, V. S. Ilchenko, D. Eliyahu, A. A. Savchenkov, A. B. Matsko, D. Seidel, and L. Maleki, "Ultralow noise miniature external cavity semiconductor laser," *Nat. Commun.* **6**, 7371 (2015).
- ⁵⁷P. A. Morton and M. J. Morton, "High-power, ultra-low noise hybrid lasers for microwave photonics and optical sensing," *J. Lightwave Technol.* **36**, 5048–5057 (2018).
- ⁵⁸Y. Fan, R. M. Oldenbeuving, C. G. Roeloffzen, M. Hoekman, D. Gekus, R. G. Heideman, and K.-J. Boller, "290 Hz intrinsic linewidth from an integrated optical chip-based widely tunable InP-Si₃N₄ hybrid laser," in *Conference on Lasers and Electro-Optics* (OSA Publishing, 2017), Vol. 161, p. 2013.
- ⁵⁹H. Guan, A. Novack, T. Galfsky, Y. Ma, S. Fatholouloumi, A. Horth, T. N. Huynh, J. Roman, R. Shi, M. Caverley, Y. Liu, T. Baehr-Jones, K. Bergman, and M. Hochberg, "Widely-tunable, narrow-linewidth III-V/silicon hybrid external-cavity laser for coherent communication," *Opt. Express* **26**, 7920 (2018).
- ⁶⁰A. Verdier, G. De Valicourt, R. Brenot, H. Debregeas, P. Dong, M. Earnshaw, H. Carrere, and Y. K. Chen, "Ultrawideband wavelength-tunable hybrid external-cavity lasers," *J. Lightwave Technol.* **36**, 37–43 (2018).
- ⁶¹K. Sato, N. Kobayashi, M. Namiwaka, K. Yamamoto, T. Kita, H. Yamada, and H. Yamazaki, "High output power and narrow linewidth silicon photonic hybrid ring-filter external cavity wavelength tunable lasers," in *European Conference on Optical Communication, ECOC (Systematic Paris Region Systems and ICT Cluster)* (IEEE, 2014), pp. 1–3.
- ⁶²C. Xiang, P. A. Morton, and J. E. Bowers, "Ultra-narrow linewidth laser based on a semiconductor gain chip and extended Si₃N₄ Bragg grating," *Opt. Lett.* **44**, 3825 (2019).
- ⁶³D. S. Elliott, R. Roy, and S. J. Smith, "Extracavity laser band-shape," *Phys. Rev. A* **26**, 12–18 (1982).
- ⁶⁴G. M. St phan, T. T. Tam, S. Blin, P. Besnard, and M. T tu, "Laser line shape and spectral density of frequency noise," *Phys. Rev. A* **71**, 043809 (2005).
- ⁶⁵G. Di Domenico, S. Schilt, and P. Thomann, "Simple approach to the relation between laser frequency noise and laser line shape," *Appl. Opt.* **49**, 4801 (2010).
- ⁶⁶A. L. Schawlow and C. H. Townes, "Infrared and optical masers," *Phys. Rev.* **112**, 1940 (1958).
- ⁶⁷K. Kikuchi, "Effect of 1/f-type FM noise on semiconductor-laser linewidth residual in high-power limit," *IEEE J. Quantum Electron.* **25**, 684–688 (1989).
- ⁶⁸K. Kikuchi, "Impact of 1/f-type FM noise on coherent optical communications," *Electron. Lett.* **23**, 885 (1987).
- ⁶⁹T. Okoshi, K. Kikuchi, and A. Nakayama, "Novel method for high resolution measurement of laser output spectrum," *Electron. Lett.* **16**, 630 (1980).
- ⁷⁰L. Coldren, S. Corzine, and M. Mashanovitch, *Diode Lasers and Photonic Integrated Circuits*, 2nd ed. (John Wiley and Sons, 2012).
- ⁷¹L. B. Mercer, "1/f frequency noise effects on self-heterodyne linewidth measurements," *J. Lightwave Technol.* **9**, 485–493 (1991).
- ⁷²S. Camatel and V. Ferrero, "Narrow linewidth CW laser phase noise characterization methods for coherent transmission system applications," *J. Lightwave Technol.* **26**, 3048–3055 (2008).
- ⁷³W. V. Sorin, K. W. Chang, G. A. Conrad, and P. R. Hernday, "Frequency domain analysis of an optical FM discriminator," *J. Lightwave Technol.* **10**, 787–793 (1992).
- ⁷⁴D. R. Hj lme, A. R. Mickelson, and R. G. Beausoleil, "Semiconductor laser stabilization by external optical feedback," *IEEE J. Quantum Electron.* **27**, 352–372 (1991).
- ⁷⁵C. H. Henry, "Theory of linewidth of semiconductor lasers," *IEEE J. Quantum Electron.* **18**, 259 (1982).
- ⁷⁶H. Sato and J. Ohya, "Theory of spectral linewidth of external cavity semiconductor lasers," *IEEE J. Quantum Electron.* **22**, 1060–1063 (1986).
- ⁷⁷A. Yariv, *Quantum Electronics* (John Wiley & Sons, 1989).
- ⁷⁸M. Tran, D. Huang, T. Komljenovic, J. Peters, A. Malik, and J. Bowers, "Ultra-low-loss silicon waveguides for heterogeneously integrated silicon/III-V photonics," *Appl. Sci.* **8**, 1139 (2018).
- ⁷⁹E. Patzak, A. Sugimura, S. Saito, T. Mukai, and H. Olesen, "Semiconductor laser linewidth in optical feedback configurations," *Electron. Lett.* **19**, 1026 (1983).
- ⁸⁰R. F. Kazarinov and C. H. Henry, "The relation of line narrowing and chirp reduction resulting from the coupling of a semiconductor laser to a passive resonator," *IEEE J. Quantum Electron.* **23**, 1401–1409 (1987).
- ⁸¹K. Vahala and A. Yariv, "Detuned loading in coupled cavity semiconductor lasers—Effect on quantum noise and dynamics," *Appl. Phys. Lett.* **45**, 501–503 (1984).
- ⁸²M. Osinski and J. Buus, "Linewidth broadening factor in semiconductor lasers—An overview," *IEEE J. Quantum Electron.* **23**, 9 (1987).
- ⁸³C. T. Santis, Y. Vilenchik, N. Satyan, G. Rakuljic, and A. Yariv, "Quantum control of phase fluctuations in semiconductor lasers," *Proc. Natl. Acad. Sci. U. S. A.* **115**, E7896–E7904 (2018).
- ⁸⁴C. T. Santis, Y. Vilenchik, A. Yariv, N. Satyan, and G. Rakuljic, "Sub-kHz quantum linewidth semiconductor laser on silicon chip," in *CLEO: 2015 Postdeadline Paper Digest* (OSA, 2015), Vol. 1, p. JTh5A.7.
- ⁸⁵Z. Zhang, H. Wang, N. Satyan, G. Rakuljic, C. T. Santis, and A. Yariv, "Coherent and incoherent optical feedback sensitivity of high-coherence Si/III-V hybrid lasers," in *Optical Fiber Communication Conference (OFC)* (OSA Publishing, 2019), Vol. 1, p. W4E.3.

- ⁸⁶K. Zou, Z. Zhang, P. Liao, H. Wang, Y. Cao, A. Almairan, A. Fallahpour, N. Satyan, G. Rakuljic, M. Tur, A. Yariv, and A. E. Willner, "Using a hybrid Si/III-V semiconductor laser to carry 16- and 64-QAM data signals over an 80-km distance," in *Optical Fiber Communication Conference (OFC) 2019* (OSA, 2019), Vol. 1, p. M3A.2.
- ⁸⁷S. Dhoore, G. Roelkens, and G. Morthier, "III-V-on-silicon three-section DBR laser with over 12 nm continuous tuning range," *Opt. Lett.* **42**, 1121–1124 (2017).
- ⁸⁸A. W. Fang, B. R. Koch, R. Jones, E. Lively, D. Liang, Y. H. Kuo, and J. E. Bowers, "A distributed Bragg reflector silicon evanescent laser," *IEEE Photonics Technol. Lett.* **20**, 1667–1669 (2008).
- ⁸⁹S. Keyvaninia, G. Roelkens, D. Van Thourhout, C. Jany, M. Lamponi, A. Le Liepvre, F. Lelarge, D. Make, G.-H. Duan, D. Bodel, and J.-M. Fedeli, "Demonstration of a heterogeneously integrated III-V/SOI single wavelength tunable laser," *Opt. Express* **21**, 3784–3792 (2013).
- ⁹⁰D. Huang, M. A. Tran, J. Guo, J. Peters, T. Komljenovic, A. Malik, P. A. Morton, and J. E. Bowers, "High-power sub-kHz linewidth lasers fully integrated on silicon," *Optica* **6**, 745 (2019).
- ⁹¹V. Jayaraman, Z. Chuang, and L. A. Coldren, "Theory, design, and performance of extended tuning range semiconductor lasers with sampled gratings," *IEEE J. Quantum Electron.* **29**, 1824–1834 (1993).
- ⁹²X. Wang, Y. Wang, J. Flueckiger, R. Bojko, A. Liu, A. Reid, J. Pond, N. A. F. Jaeger, and L. Chrostowski, "Precise control of the coupling coefficient through destructive interference in silicon waveguide Bragg gratings," *Opt. Lett.* **39**, 5519 (2014).
- ⁹³X. Wang, W. Shi, H. Yun, S. Grist, N. A. F. Jaeger, and L. Chrostowski, "Narrow-band waveguide Bragg gratings on SOI wafers with CMOS-compatible fabrication process," *Opt. Express* **20**, 15547 (2012).
- ⁹⁴D. T. H. Tan, K. Ikeda, and Y. Fainman, "Cladding-modulated Bragg gratings in silicon waveguides," *Opt. Lett.* **34**, 1357 (2009).
- ⁹⁵G. Jiang, R. Chen, Q. Zhou, J. Yang, M. Wang, and X. Jiang, "Slab-modulated sidewall Bragg gratings in silicon-on-insulator ridge waveguides," *IEEE Photonics Technol. Lett.* **23**, 6–8 (2011).
- ⁹⁶D. T. Spencer, M. Davenport, S. Srinivasan, J. Khurgin, P. A. Morton, and J. E. Bowers, "Low kappa, narrow bandwidth Si₃N₄ Bragg gratings," *Opt. Express* **23**, 30329 (2015).
- ⁹⁷A. D. Simard, Y. Painchaud, and S. LaRochelle, "Integrated Bragg gratings in spiral waveguides," *Opt. Express* **21**, 8953 (2013).
- ⁹⁸P. Bardella and I. Montrosset, "Analysis of self-pulsating three-section DBR lasers," *IEEE J. Sel. Top. Quantum Electron.* **11**, 361–366 (2005).
- ⁹⁹X. Pan, H. Olesen, and B. Tromborg, "A theoretical model of multielectrode DBR lasers," *IEEE J. Quantum Electron.* **24**, 2423–2432 (1988).
- ¹⁰⁰M. A. Tran, D. Huang, J. Guo, T. Komljenovic, P. A. Morton, and J. E. Bowers, "Ring-resonator based widely-tunable narrow-linewidth Si/InP integrated lasers," *IEEE J. Sel. Top. Quantum Electron.* **26**, 1–14 (2020).
- ¹⁰¹H. Jayatilaka, H. Shoman, L. Chrostowski, and S. Shekhar, "Photoconductive heaters enable control of large-scale silicon photonic ring resonator circuits," *Optica* **6**, 84 (2019).
- ¹⁰²Y. Li and A. W. Poon, "Active resonance wavelength stabilization for silicon microring resonators with an in-resonator defect-state-absorption-based photodetector," *Opt. Express* **23**, 360 (2015).
- ¹⁰³E. D. Black, "An introduction to Pound–Drever–Hall laser frequency stabilization," *Am. J. Phys.* **69**, 79–87 (2001).
- ¹⁰⁴M. H. Idjadi and F. Aflatouni, "Integrated Pound–Drever–Hall laser stabilization system in silicon," *Nat. Commun.* **8**, 1209 (2017).
- ¹⁰⁵S. B. Papp, private communication (unpublished, 2019).
- ¹⁰⁶W. Zhang, L. Stern, D. Carlson, D. Bopp, Z. Newman, S. Kang, J. Kitching, and S. B. Papp, "Ultrannarrow linewidth photonic-atomic laser," in *Frontiers in Optics + Laser Science APS/DLS* (OSA Publishing, 2019), pp. 1–7.
- ¹⁰⁷Z. Zhang, D. Jung, J. C. Norman, W. W. Chow, and J. E. Bowers, "Linewidth enhancement factor in InAs/GaAs quantum dot lasers and its implication in isolator-free and narrow linewidth applications," *IEEE J. Sel. Top. Quantum Electron.* **25**, 1–9 (2019).
- ¹⁰⁸T. Septon, S. Gosh, A. Becker, V. Sichkovskyi, F. Schnabel, A. Rippien, J. P. Reithmaier, and G. Eisenstein, "Narrow linewidth InAs/InP quantum dot DFB laser," in *2019 Optical Fiber Communications Conference and Exhibition* (OSA Publishing, 2019), p. W3A.8.
- ¹⁰⁹J. Duan, H. Huang, Z. G. Lu, P. J. Poole, C. Wang, and F. Grillot, "Narrow spectral linewidth in InAs/InP quantum dot distributed feedback lasers," *Appl. Phys. Lett.* **112**, 121102 (2018).
- ¹¹⁰A. J. Zilkie, P. Srinivasan, A. Trita, T. Schrans, G. Yu, J. Byrd, D. A. Nelson, K. Muth, D. Leroese, M. Alalusi, K. Masuda, M. Ziebell, H. Abediasl, J. Drake, G. Miller, H. Nykanen, E. Kho, Y. Liu, H. Liang, H. Yang, F. H. Peters, A. S. Nagra, and A. G. Rickman, "Multi-micron silicon photonics platform for highly manufacturable and versatile photonic integrated circuits," *IEEE J. Sel. Top. Quantum Electron.* **25**, 1–13 (2019).
- ¹¹¹X. Ji, F. A. S. Barbosa, S. P. Roberts, A. Dutt, J. Cardenas, Y. Okawachi, A. Bryant, A. L. Gaeta, and M. Lipson, "Ultra-low-loss on-chip resonators with sub-milliwatt parametric oscillation threshold," *Optica* **4**, 619 (2017).
- ¹¹²J. F. Bauters, M. J. R. Heck, D. D. John, J. S. Barton, C. M. Bruinink, A. Leinse, R. G. Heideman, D. J. Blumenthal, and J. E. Bowers, "Planar waveguides with less than 0.1 dB/m propagation loss fabricated with wafer bonding," *Opt. Express* **19**, 24090–24101 (2011).
- ¹¹³M. W. Puckett, J. Wang, G. Brodnik, J. Wu, K. Nelson, and D. Blumenthal, "Silicon nitride ring resonators with 0.123 dB/m loss and Q-factors of 216 million for nonlinear optical applications," in *2019 Conference on Lasers and Electro-Optics Europe and European Quantum Electronics Conference* (OSA Publishing, 2019), p. ce_11_3.
- ¹¹⁴B. Milivojevic, C. Raabe, A. Shastri, M. Webster, P. Metz, S. Sunder, B. Chatin, S. Wiese, B. Dama, and K. Shastri, "112Gb/s DP-QPSK transmission over 2427km SSMF using small-size silicon photonic IQ modulator and low-power CMOS driver," in *Optical Fiber Communication Conference/National Fiber Optic Engineers Conference 2013* (OSA Publishing, 2013), p. OTh1D.1.
- ¹¹⁵A. Liu, R. Jones, L. Liao, D. Samara-Rubio, D. Rubin, O. Cohen, R. Nicolaescu, and M. Paniccia, "A high-speed silicon optical modulator based on a metal–oxide–semiconductor capacitor," *Nature* **427**, 615–618 (2004).
- ¹¹⁶J.-H. H. Han, F. Boeuf, J. Fujikata, S. Takahashi, S. Takagi, M. Takenaka, S. Takahashi, F. Boeuf, J.-H. H. Han, and S. Takagi, "Efficient low-loss InGaAsP/Si hybrid MOS optical modulator," *Nat. Photonics* **11**, 486–490 (2017).
- ¹¹⁷T. Hiraki, T. Aihara, K. Hasebe, K. Takeda, T. Fujii, T. Kakitsuka, T. Tsuchizawa, H. Fukuda, and S. Matsuo, "Heterogeneously integrated III-V/Si MOS capacitor Mach-Zehnder modulator," *Nat. Photonics* **11**, 482–485 (2017).
- ¹¹⁸E. Rubiola, *Phase Noise and Frequency Stability in Oscillators*, The Cambridge RF and Microwave Engineering Series (Cambridge University Press, 2009).